

## RESEARCH ARTICLE

10.1002/2014JB011547

## Key Points:

- We estimate monthly GRACE gravity fields with harmonics and constrained mascons
- Mascon and spherical harmonic solutions are compared globally and regionally
- Bayesian a priori conditioning of the mascons yields significant improvement

## Correspondence to:

D. N. Wiese,  
david.n.wiese@jpl.nasa.gov

## Citation:

Watkins, M. M., D. N. Wiese, D.-N. Yuan, C. Boening, and F. W. Landerer (2015), Improved methods for observing Earth's time variable mass distribution with GRACE using spherical cap mascons, *J. Geophys. Res. Solid Earth*, 120, 2648–2671, doi:10.1002/2014JB011547.

Received 20 AUG 2014

Accepted 23 FEB 2015

Accepted article online 26 FEB 2015

Published online 7 APR 2015

## Improved methods for observing Earth's time variable mass distribution with GRACE using spherical cap mascons

Michael M. Watkins<sup>1</sup>, David N. Wiese<sup>1</sup>, Dah-Ning Yuan<sup>1</sup>, Carmen Boening<sup>1</sup>, and Felix W. Landerer<sup>1</sup>
<sup>1</sup>Jet Propulsion Laboratory, California Institute of Technology, Pasadena, California, USA

**Abstract** We discuss several classes of improvements to gravity solutions from the Gravity Recovery and Climate Experiment (GRACE) mission. These include both improvements in background geophysical models and orbital parameterization leading to the unconstrained spherical harmonic solution JPL RL05, and an alternate JPL RL05M mass concentration (mascon) solution benefitting from those same improvements but derived in surface spherical cap mascons. The mascon basis functions allow for convenient application of a priori information derived from near-global geophysical models to prevent striping in the solutions. The resulting mass flux solutions are shown to suffer less from leakage errors than harmonic solutions, and do not necessitate empirical filters to remove north-south stripes, lowering the dependence on using scale factors (the global mean scale factor decreases by 0.17) to gain accurate mass estimates. Ocean bottom pressure (OBP) time series derived from the mascon solutions are shown to have greater correlation with in situ data than do spherical harmonic solutions (increase in correlation coefficient of 0.08 globally), particularly in low-latitude regions with small signal power (increase in correlation coefficient of 0.35 regionally), in addition to reducing the error RMS with respect to the in situ data (reduction of 0.37 cm globally, and as much as 1 cm regionally). Greenland and Antarctica mass balance estimates derived from the mascon solutions agree within formal uncertainties with previously published results. Computing basin averages for hydrology applications shows general agreement between harmonic and mascon solutions for large basins; however, mascon solutions typically have greater resolution for smaller spatial regions, in particular when studying secular signals.

## 1. Introduction

Since launch on 17 March 2002, the Gravity Recovery and Climate Experiment (GRACE) has provided pioneering observations of global mass flux that have contributed significantly to our understanding of large-scale changes in polar ice, ground water storage, and ocean mass distribution [Chambers, 2006; Rodell et al., 2009; Velicogna, 2009; Luthcke et al., 2013].

The vast majority of these results have been derived from analysis of global gravity fields that have been solved for in terms of spherical harmonic basis functions. Spherical harmonics have been well studied and widely used in satellite geodesy for several decades, based largely on the computational efficiency of the parameterization, and because the satellite sensitivity is dependent on the spatial wavelength of the mass variations which is implicit in the harmonic basis function. However, unconstrained harmonic solutions from GRACE have typically suffered from poor observability of east-west gradients, resulting in the so-called “stripes” that are conventionally removed via empirical smoothing and/or “destriping” algorithms. Although quite effective, especially for larger spatial scales, the destriping also removes some real geophysical signal along with the stripes, and the size, shape, and orientation of the signals strongly affect the effectiveness of destriping.

In addition to spherical harmonics solutions, there have been three classes of GRACE mass concentration (mascon) solutions in the literature that have been used to study time variable gravity. The first class of mascon solution is one in which an analytic expression for the mass concentration function is provided, and explicit partial derivatives relating the intersatellite range-rate measurements to the analytic mascon formulation are used to directly estimate mass variations. An example of this first type of mascon solution is found in Ivins et al. [2011], which is based on a mascon approach outlined in Watkins et al. [2005] in which spherical cap mascons are estimated directly from range accelerations to derive mass fluxes. The second class of mascon solution found in the literature comes from the group at NASA Goddard Space Flight Center

[Luthcke *et al.*, 2006a; Rowlands *et al.*, 2010; Sabaka *et al.*, 2010; Luthcke *et al.*, 2013]. This type of mascon solution shares commonality with the first type of mascon solution in the sense that the mascon basis functions are directly related to the intersatellite range-rate measurements through explicit partial derivatives, which are used in the gravity estimation. The difference is that each mascon basis function is represented by a finite truncated spherical harmonic expansion, rather than an analytical expression, such that the functional representation of each mascon has signal power outside of the mascon boundary. Finally, the third class of so-called “mascon” solutions are when users fit mass elements to spherical harmonic coefficients (from spherical harmonic GRACE solutions) as a form of postprocessing to remove correlated error; in essence, this is a form of destriping, as discussed above. These are not true mascon solutions in the sense that there is no direct relation between the formulation of the mass elements and the intersatellite range-rate measurements (i.e., there are no explicit partial derivatives relating the observations to the state). Examples of this type of mascon solution include Jacob *et al.* [2012], Schrama *et al.* [2014], and Velicogna *et al.* [2014]. Both the first and second types of mascon solutions described above have the unique advantage of being able to simultaneously adjust all state parameters when estimating the gravity potential.

In this paper, we describe and evaluate a state-of-the-art unconstrained harmonic solution, JPL RL05, and also derive a new mascon solution, JPL RL05M, which uses surface spherical cap mascons to directly estimate mass variations from the intersatellite range-rate measurements. Note that throughout this paper, we refer to these two solutions as JPL RL05 and JPL RL05M; however, when downloading the solutions from the Physical Oceanography Distributed Active Archive Center (PODAAC) and GRACE Tellus websites, the solutions are referred to as JPL RL05.1 and JPL RL05.1M to reflect minor updates in processing as well as a correction to a brief error in the dealiasing models which occurred in 2013. This new mascon solution falls into the first class of mascon solutions described above, as it explicitly relates the intersatellite range-rate measurements to an analytic formulation of surface spherical cap mascons, similar to that described in Ivins *et al.* [2011]. The primary difference with respect to Ivins *et al.* [2011] is that we use range-rate measurements as the observations rather than range accelerations, and more importantly, we take advantage of the convenient application of geophysically based a priori conditioning to prevent striping that mascons allow, as discussed in Rowlands *et al.* [2010], Sabaka *et al.* [2010], and Luthcke *et al.* [2013]. It should be noted, however, that the regularization applied here is fundamentally different than that described in Rowlands *et al.* [2010], Sabaka *et al.* [2010], and Luthcke *et al.* [2013], as these solutions focused on the derivation of an a priori covariance matrix which is tailored for recovery of ice mass variations. Our choice of regularization uses a combination of near-global geophysical models in combination with altimetry observations to gain accurate mass flux estimates globally, rather than focusing on estimating a particular subset of mass variations. We do note that the development of our mascon solution was primarily motivated by the potential to improve estimates of mass fluxes in the ocean, which are small in amplitude and difficult to detect.

In summary, the key advantages to our mascon approach over existing methods are twofold: (1) for the first time, a mascon solution is formed in which range-rate observations are explicitly linked to an analytic mascon formulation through partial derivatives, and (2) for the first time, we show the development of a global a priori covariance matrix for a mascon solution which is well suited to recover global mass fluxes, in particular over the ocean. In this paper, we demonstrate several advantages to this approach over existing GRACE solutions, and summarize key global mass flux results in ice mass, hydrology, and ocean circulation.

## 2. Theory

### 2.1. Spherical Harmonics Gravity Model

The gravitational potential due to a nonspherical central body can be expressed in terms of a spherical harmonic expansion with respect to a body-fixed reference frame as [Heiskanen and Moritz, 1967; Kaula, 1966]

$$U(r, \varphi, \lambda) = \frac{Gm}{r} + \frac{Gm}{r} \sum_{l=1}^{\infty} \sum_{m=0}^l \left( \frac{a_e}{r} \right)^l \bar{P}_{lm}(\sin \varphi) [\bar{C}_{lm} \cos \lambda + \bar{S}_{lm} \sin \lambda], \quad (1)$$

where  $\bar{C}_{lm}$ ,  $\bar{S}_{lm}$  are fully normalized spherical harmonic coefficients of degree  $l$  and order  $m$ ;  $\bar{P}_{lm}(\sin \varphi)$  are the fully normalized associated Legendre functions of degree  $l$  and order  $m$ ;  $Gm$  is the gravitational constant of Earth;  $a_e$  is the mean equatorial radius of the Earth; and  $r$ ,  $\varphi$ ,  $\lambda$  are radial distance, latitude, and longitude of the spacecraft.

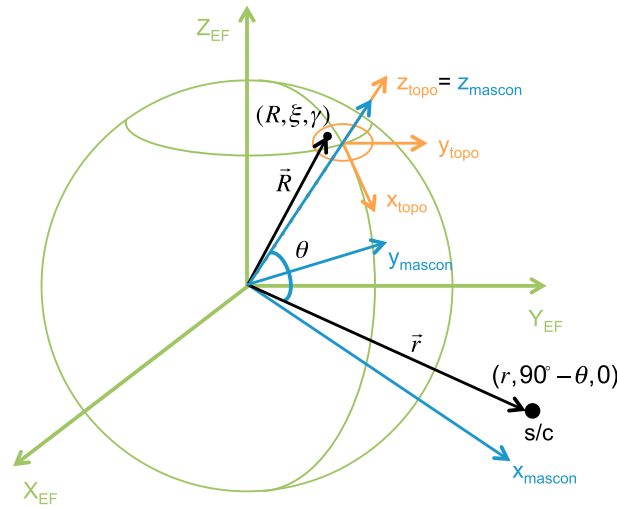


**Figure 1.** Spherical cap mascon model on the surface of a sphere and definition of coordinate systems used.

The fully normalized spherical harmonic coefficients are dimensionless quantities via the introduction of  $Gm$  and  $a_e$  into the formulation. Since harmonic coefficients are integrals of mass distribution of the central body with respect to a body-fixed coordinate system, they would be time invariant if the central body were rigid.

## 2.2. Surface Spherical Cap Mass Concentration Model

The use of discrete masses to describe the gravitational field is a well-known concept from classical geodesy. After the initial discovery of lunar mass concentrations (mascons) [Muller and Sjogren, 1968], point mass and flat disk mascon solutions to represent the lunar gravitational field were developed [Wong et al., 1971]. Following the same concept, the time-varying

gravity field of the Earth caused by surface mass redistribution can be modeled by a globally distributed mascon field in a finite time interval with respect to a mean, where each mascon with uniform mass density at a predetermined location represents an addition or reduction of surface mass.

Wong et al. [1971] indicated that the point mass and flat disk models have limitations when fitting the tracking data for lunar orbiters. Thus, a spherical cap mascon model was derived to better represent the finite extent of the surface mass layer on a spherical surface. The gravitational acceleration of a spacecraft due to a spherical cap mascon is summarized below, and an illustration of the coordinate systems used is shown in Figure 1. Each mascon region is expressed as a spherical cap on the surface of a sphere. The location of the spherical cap mascon on the surface is fixed by giving the body-fixed spherical coordinates  $(r, \varphi, \lambda)$  of the center of the mascon. Each mascon is also assigned a  $Gm$  to specify the mass, and a solid angle from the center to the edge of the spherical cap,  $\alpha$ , to specify the size. The coordinate transformation matrix,  $B$ , from the body-fixed system (Figure 1; green) to the topographic coordinate system (Figure 1; orange) is

$$B = R_y(\varphi - 90^\circ)R_z(\lambda), \quad (2)$$

where  $R_y$  and  $R_z$  are the rotation matrices about the Earth-Fixed (EF)  $y$  axis ( $Y_{EF}$ ) and  $z$  axis ( $Z_{EF}$ ). The gravitational acceleration acting on the spacecraft from a mascon is then computed in the local mascon coordinate system (Figure 1; blue) with the  $z$  axis ( $Z_{mascon}$ ) along the body center to the mascon center, and with the  $x$  axis ( $X_{mascon}$ ) chosen such that the spacecraft is in the  $xz$  plane. The spacecraft position vector in local mascon coordinates is represented as

$$\vec{r} = (r \sin \theta, 0, r \cos \theta), \quad (3)$$

where  $\theta$  is the colatitude. The position vector of a point mass on a spherical cap in local mascon coordinates is represented as

$$\vec{R} = (R \sin \gamma \cos \zeta, R \sin \gamma \sin \zeta, R \cos \gamma), \quad (4)$$

and the distance,  $d$ , between the spacecraft and this point mass on the spherical cap mascon is given by

$$d^2 = r^2 + R^2 - 2Rr(\sin \gamma \cos \zeta \sin \theta + \cos \gamma \cos \theta), \quad (5)$$

The gravitational potential of the mascon at the spacecraft position is then calculated by integrating over the entire spherical cap mascon surface and is given by

$$V = R^2 \sigma \int_0^\alpha \sin \gamma \int_0^{2\pi} \frac{d\zeta}{d} d\gamma. \quad (6)$$

The gravitational acceleration on the spacecraft expressed in the local mascon coordinate system is a function of the calculated gravitational potential and is given by

$$(a_r, a_\theta, a_\phi) = \left( \frac{\partial V}{\partial r}, 0, \frac{1}{r} \frac{\partial V}{\partial \theta} \right). \quad (7)$$

The gravitational acceleration components  $a_r$  and  $a_\theta$  are then computed as

$$\begin{aligned} a_r &= -\sigma t^3 \left( \frac{l_2}{t} - \cos \theta \cdot l_1 - \sin \theta \cdot l_3 \right) \\ a_\theta &= -\sigma t^3 (\sin \theta \cdot l_1 - \cos \theta \cdot l_3) \end{aligned} \quad (8)$$

where  $t = R/r$  and the density function of a mascon, defined as the mascon  $Gm$  divided by its area, is computed as

$$\sigma = \frac{Gm}{2\pi(1 - \cos \alpha)R^2}. \quad (9)$$

The integrals  $l_1$ ,  $l_2$ , and  $l_3$  are defined as

$$\begin{aligned} l_1 &= \int_0^\alpha \sin \gamma \cos \gamma \cdot J_1(\gamma, \theta, r) d\gamma \\ l_2 &= \int_0^\alpha \sin \gamma \cdot J_1(\gamma, \theta, r) d\gamma \\ l_3 &= \int_0^\alpha \sin^2 \gamma \cdot J_2(\gamma, \theta, r) d\gamma. \end{aligned} \quad (10)$$

The integrands  $J_1$  and  $J_2$  are functions of the complete elliptic integral of the second kind  $E(k)$  and the complete elliptic integral of the first kind  $K(k)$ , and are defined as

$$\begin{aligned} J_1(\gamma, \theta, r) &= \frac{m'}{\sqrt{l' + 1}(l' + 1)} E(k) \\ J_2(\gamma, \theta, r) &= \frac{m'}{\sqrt{l' + 1}(l' + 1)l'} [E(k) - (1 - l')K(k)], \end{aligned} \quad (11)$$

where parameters  $m'$ ,  $l'$ , and  $k$  are

$$\begin{aligned} n &= 1 + t^2 - 2t \cos \theta \cos \gamma \\ m' &= 4/n^{3/2} \\ l' &= 2t \sin \theta \sin \gamma / n \\ k^2 &= 2l'/(l' + 1). \end{aligned} \quad (12)$$

The gravitational acceleration computed in the local mascon coordinate system is then rotated to the final inertial system for spacecraft orbit integration. The partial derivatives of the gravitational acceleration with respect to the spacecraft state and model parameters have been derived [Sunseri, 2010] and implemented in the Orbit Determination Program (ODP) [Moyer, 1971, 2000] of the Jet Propulsion Laboratory.

### 3. The Gravity Estimation Process: General Approach and Models

The monthly gravity field solutions from GRACE are derived using a least squares procedure implemented as a parallelized square-root information filter (SRIF) with the ODP software variant referred to as MIRAGE. The GRACE Level 1B (L1B) data products used in this processing are described in Case *et al.* [2010]. The L1B GRACE data used are version 2 of the Level 1B products which have several improvements over the version 1 release. One particular improvement is updated knowledge of the relative alignment between the science instruments (K-Band Ranging system antenna boresight, accelerometer, and star camera) through reanalysis of calibration maneuvers.

#### 3.1. Reference Systems

The inertial coordinate system used for orbit integration is the geocentric, Earth mean equator and vernal equinox system at J2000.0, which is consistent with the International Earth Rotation Service (IERS) celestial reference frame labeled International Celestial Reference Frame 2. The Earth-fixed coordinate system is consistent with the IERS terrestrial reference frame labeled ITRF2008 [Petit and Luzum, 2010]. The adopted ephemerides for the Sun, Moon, and planetary systems are the JPL DE421 planetary ephemeris [Folkner *et al.*, 2009]. The JPL Earth Orientation Parameters products are derived from the very long baseline interferometry

**Table 1.** Summary of Background Force Models Used in GRACE Data Processing<sup>a</sup>

Force Model	Parameters and Remarks	Description
Static Earth Gravity	GIF48	Degree/order 180
Solid tides	IERS2010 nonelastic Earth	Degree 2, 3, and 4
Ocean tides	GOT4.7 and self-consistent equilibrium long-period tide	Convolution formalism to degree/order 90
Solid pole tide	IERS2010 nonelastic Earth	IERS2010 mean pole
Ocean pole tide	IERS2010	Degree/order 90
Nontidal atmosphere and ocean dealiasing	ECMWF atmosphere and baroclinic OMCT ocean model	Degree/order 100
Third-body perturbations from Sun, Moon, and planets	DE-421	
General relativity	Point mass perturbation, geodesic and Lense-Thirring	Sun and Earth
Nongravitational forces	5 s accelerometer data	GRACE Level-1 product

<sup>a</sup>Full model details are available in *Watkins and Yuan* [2012].

and lunar laser ranging observations [*Folkner et al.*, 1993], which include Earth rotation and polar motion calibrations, as well as nutation correction parameters necessary to determine inertial station locations to the level of few centimeters.

### 3.2. Dynamic Models

The gravitational potential due to the nonspherical shape of the Earth can be expressed in terms of a spherical harmonic expansion with respect to a body-fixed reference frame as shown in equation (1). We use the static Earth gravity field model GIF48 [*Ries et al.*, 2011] as the nominal mean model and set degree one harmonic coefficients to zero since the origin of the coordinate system is chosen to be the center of mass of the Earth.

Third-body gravitational perturbations on the spacecraft are computed using the Newtonian point mass model for the Sun, planets, and Moon. The point mass relativistic perturbations due to the Sun and Earth, the geodesic precession due to the Earth motion, and Lense-Thirring precession due to the Earth rotation are included in the force model for calculating the GRACE orbit [*Moyer*, 2000].

The gravitational effects of the solid body tides due to the Sun and Moon are included in the force model, and the Love numbers from IERS 2010 [*Petit and Luzum*, 2010] are adopted. The convolution formalism for ocean tidal contributions to the geopotential is used [*Desai and Yuan*, 2006], where the convolution weights to degree and order 90 are derived from GOT4.7 [*Ray*, 1999] for monthly, fortnightly, diurnal, and semidiurnal constituents and self-consistent quasi-equilibrium tides for semiannual and annual constituents.

The short period nontidal variability in the atmosphere and oceans is removed (“dealiasing”) through using the AOD1B product [*Dobslaw et al.*, 2013] as a background model. For JPL RL05, we use the AOD1B RL05, based upon European Centre for Medium-Range Weather Forecasts (ECMWF) and the baroclinic Ocean Model for Circulation and Tides (OMCT). The details of this product and its generation are given in the *AOD1B Description Document* (GRACE 327–750). A detailed description of the background force models used in the orbit determination and gravity field recovery is summarized in Table 1.

### 3.3. Measurement Models

The two primary observation types processed are satellite-to-satellite instantaneous range-rate measurements derived from one-way phase of the K band ranging system [*Kim*, 2000; *Wu et al.*, 2006], along with GPS pseudorange and phase measurements. The orbits of the GPS spacecraft and the GPS transmitter clock biases are provided by the FLINN products of JPL [*Desai et al.*, 2011]. The GPS antenna phase center to center of gravity offset is modeled as a constant vector, and antenna calibration maps are used for both the transmitter and receiver [*Montenbruck et al.*, 2009]. General relativity propagation delay due to the reduction of the speed of light by the Sun [*Holdridge*, 1967; *Moyer*, 1971] is applied for the GPS one-way light time calculations. The observations used during this process are summarized in Table 2.

**Table 2.** Summary of Observation Types Used to Process Monthly Gravity Solutions

Observations	Version	Sampling Rate
GPS ionosphere free pseudorange and phase	GRACE Level 1 version 2	5 min
K band range rate	GRACE Level 1 version 2	5 s



**Table 3.** Parameters Estimated During Gravity Inversion

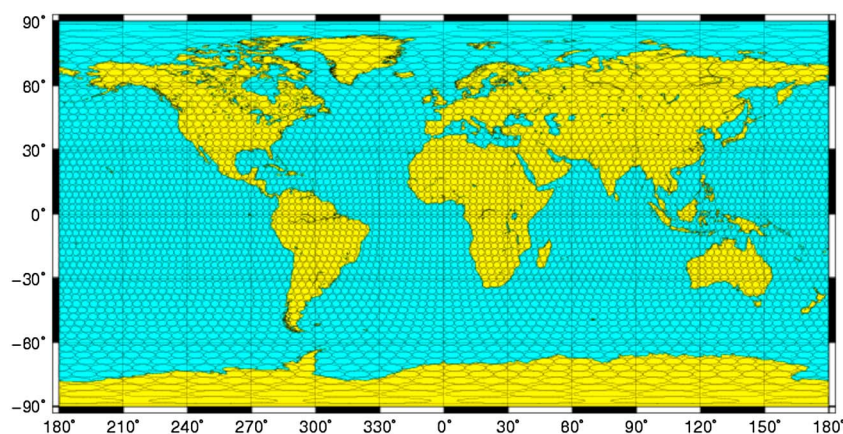
Parameter	Remarks	Frequency of Estimate
Satellite state	Position and velocity	Daily
Accelerometer bias	Three components	Daily
GPS phase bias	Constant	Each GPS-GRACE pass
KBR range-rate biases	Constant, drift, and once per revolution	One orbital revolution (5400 s)
Spherical harmonics or mascon $Gm$ parameters	$90 \times 90$ or $60 \times 60$ ; based on monthly ground track and data coverage or $3^\circ$ equal-area spherical cap (4551 mascons)	Monthly
Accelerometer scale	$X$ and $Y$ components	Monthly

### 3.4. Estimated Parameters

After converging the orbits with a reduced number of parameters (only local parameters described below) to ensure linearity in the gravity solution step, we compute partial derivatives for gravity harmonics (or mascon parameters), accelerometer instrument scale factors, accelerometer biases, GRACE spacecraft state (position and velocity), and KBR and GPS nuisance parameters (Table 3). For each daily orbital arc, sets of SRIF equations derived from GPS data and KBR data are computed separately. These are then combined into a single set of global gravity harmonic or mascon parameters along with a single accelerometer scale factor to gain the full set of information equations for each month. The local parameters estimated simultaneously with the global parameters (spherical harmonics/mascons and accelerometer scale factor) are: (1) GRACE initial state for daily arcs, (2) GPS phase biases, (3) KBR biases, and (4) accelerometer biases.

The accelerometer scale factor appears to be relatively stable, and the choice was made to estimate a scale factor for the  $x$  axis and  $y$  axis each month. A scale was not estimated for the  $z$  axis as it was found to be correlated with the  $x$  axis, even on monthly timescales. The accelerometer biases, however, display some drift within a month, and this has been accommodated by estimating the bias along each axis for each daily batch of data. The KBR and accelerometer errors are expected to cause drifts in measurement residuals on timescales longer than the orbital period, and the estimated biases are designed to accommodate this longer period error [Kim, 2000]. The time interval for the piecewise constant bias terms was chosen by experiment to be sufficiently long so that the higher frequencies associated with the geopotential harmonics are not absorbed.

When combining the daily SRIF equations for GPS and KBR measurements, the weights of the individual information equations are independently adjusted using an iterative optimal weighting procedure [Yuan, 1991]. It should be noted that when estimating mascon parameters, only the KBR SRIF equations are used to form the monthly matrix, as it was found that the addition of the GPS SRIF equations contributes to additional noise in the gravity solution. The exclusion of the GPS data leads to poor estimation of long wavelength features in the gravity field since the estimate of the satellite state suffers, and we therefore replace degree 2 and 3 coefficients in the mascon solution with those derived from the JPL RL05 harmonic solution. It should be noted that other gravity solutions also use KBR data only to form their solution [Luthcke et al., 2006b, 2013].


**Figure 2.** Global  $3^\circ$  equal-area spherical cap mascons used for JPL RL05M.

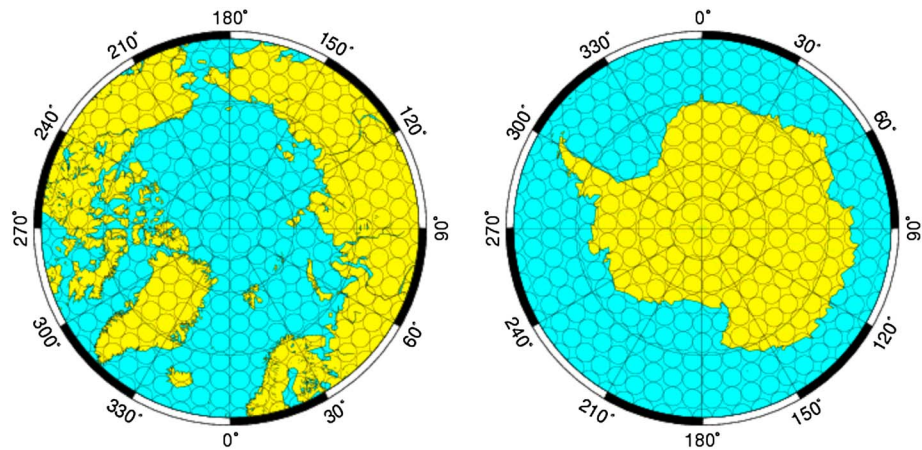


**Figure 3.** Global 3° equal-area spherical cap mascons in polar views.

### 3.5. Treatment of the Mascon Solution

The native mascon solution consists of a collection of spherical cap unit masses ( $Gm$ ) which have been estimated by the filter. This set of basis functions naturally does not cover the entire surface of the Earth, as there exist gaps in between the placement of each spherical cap (seen in Figures 2 and 3). We have verified via numerous tests and simulations that the gravity signal from the small regions not explicitly included in the spherical caps are completely and predictably absorbed by the nearest neighboring mascons, and as such the full signal magnitude is estimated and accounted for in our processing.

The mascon solution is then decomposed into a high-degree nondimensional spherical harmonics representation, and the low degrees (2 and 3) are replaced with those derived from JPL RL05 harmonics, as discussed above. It should also be mentioned that at this point we apply the loading correction to our mascon solution in the same fashion that it is applied to the harmonic solution in order to study surface loads. Although we are estimating surface spherical cap mascons, the filter knows nothing of elastic loading, and as such is simply estimating the geopotential change on the surface of the Earth at each location. In order to study surface loads, a loading correction must therefore be applied.

## 4. Spatial Constraints Applied to the Mascon Solution

As discussed in section 3.0, the monthly gravity solution is obtained by solving the well-known weighted least squares problem, given by [Tapley *et al.*, 2004]

$$\left(H^T W H + \bar{P}_0^{-1}\right) \hat{x}_0 = H^T W y + \bar{P}_0^{-1} \bar{x}_0, \quad (13)$$

where  $H$  is a matrix of partial derivatives relating the observations ( $y$ ), given in Table 2, to the state parameters ( $\hat{x}_0$ ), given in Table 3,  $W$  is a weighting matrix for the observations,  $\bar{x}_0$  is the a priori value of the state parameters, and  $\bar{P}_0$  represents the a priori uncertainty on the state parameters and is given by

$$\bar{P}_0 = \begin{bmatrix} \sigma_i^2 & \rho_{ij} \sigma_i \sigma_j & \cdots \\ \rho_{ij} \sigma_i \sigma_j & \sigma_j^2 & \\ \vdots & & \ddots \end{bmatrix}. \quad (14)$$

In equation (14),  $\sigma_i$  is the a priori uncertainty on the  $i$ th mascon,  $\sigma_j$  is the a priori uncertainty on the  $j$ th mascon, and  $\rho_{ij}$  is the correlation coefficient between the  $i$ th and  $j$ th mascons.

When solving for gravity variations in unconstrained spherical harmonic basis functions,  $\bar{P}_0 = 0$ ,  $\bar{x}_0 = 0$ , and  $\hat{x}_0$  is a vector of  $C_{lm}$  and  $S_{lm}$  coefficients. This parameterization of the inversion problem ultimately results in gravity solutions from GRACE with longitudinal “stripe patterns” that dominate geophysical signals. These stripes are primarily caused by poor observability of the east-west gradients due to the north-south

orientation of the satellite ground tracks, allowing almost any orbit error to leak into the solution and cause the stripes. Many users remove the striping errors by applying spectral filters in postprocessing of the data, the most common of which include Gaussian smoothing [Wahr *et al.*, 1998] and a destriping algorithm [Swenson and Wahr, 2006], which damp errors in high-degree coefficients and remove correlated errors in coefficients of a fixed order and the same parity of degree, respectively. This approach has been shown to be generally quite effective, but it also removes the component of real geophysical signal that partially mimics N-S patterns [Landerer and Swenson, 2012].

An alternate method to suppress the striping errors is to design a nonzero  $\bar{P}_0$  matrix to force suppression during the least squares inversion rather than after the fact. Since  $\bar{P}_0$  is expressed in terms of the gravity state variables, this technique has the unique advantage of being able to include real, geophysical information in the Bayesian sense as part of the solution rather than relying on empirical algorithms such as globally constant spatial correlation or other ad hoc approaches such as destriping. These Bayesian constraints are also able to simultaneously affect the estimate of the spacecraft state and other nuisance parameters listed in Table 3 that are inherently correlated with the gravity solution. The disadvantages to this technique are that it is computationally more expensive, it requires significantly more expertise and geophysical information to implement, and it is more difficult for a user to quantify the amount of signal suppression which occurs. There have been several attempts at developing nonzero  $\bar{P}_0$  matrices to apply to the GRACE data. Bruinsma *et al.* [2010] developed a  $\bar{P}_0$  matrix with nonzero diagonals that are both degree and order dependent. This is a variant of the well-known Kaula constraint [Kaula, 1966] that requires high-degree coefficients to continually have less power than low-degree coefficients. Save *et al.* [2012] developed a  $\bar{P}_0$  matrix based on the L-curve criteria and showed that different  $\bar{P}_0$  matrices need to be developed based on different ground track patterns and background models used in the data processing, requiring a significant amount of effort to implement. Furthermore, Luthcke *et al.* [2013] used a nonzero  $\bar{P}_0$  matrix to constrain a type of mascon solution in which the  $\sigma$  values for each mascon are empirically determined, the  $\rho$  values are based on exponential correlation with some added constraints on geophysical boundaries, and a form of time correlation is introduced linking adjacent months together. These approaches, while successful to various degrees, have not consistently made use of our best statistical knowledge of the space and time variability of global mass fluxes to approach optimal conditioning values.

For the JPL RL05M constrained mascon solution,  $\hat{x}_0$  is specified to be a series of equal area,  $3^\circ \times 3^\circ$ , spherical cap mass concentration blocks, for which it takes 4551 to cover the surface of the Earth. Note that the definition of  $3^\circ$  is made based on equatorial area, such that the mascons cover the area of a  $3^\circ$  spherical cap placed at the equator. The placement of these mascons is seen in Figures 2 and 3. The choice of using  $3^\circ$  mascons was made after performing many tests to determine how the mascon size and the a priori spatial correlations with neighboring mascons must jointly vary as a function of latitude. This is essentially analyzing the resolution matrix for a variety of mascon sizes and a priori correlations. Note that at the equator (where ground track coverage is sparser) and at the poles (where ground track coverage is more dense), the results differ. Our tests showed that the posteriori correlation of a single  $3^\circ$  mascon at the equator with its neighbors is large enough to conclude that equatorial mascons smaller than  $3^\circ$  require significant a priori spatial correlation. Conversely, at the polar regions, the posteriori correlation of a single  $3^\circ$  mascon with its neighbors is sufficiently small to conclude that these mascons can be accurately estimated independently, therefore requiring much less a priori spatial correlation. We, therefore, pragmatically selected  $3^\circ$  as a compromise between providing good spatial resolution across the globe while requiring only modest spatial correlation, although we continue to refine this in our ongoing research, and in the future may introduce spatially varying mascon sizes.

To arrive at the final RL05M solution, a two stage process was implemented in which a “white noise” (no time correlation) solution was first generated to update geophysical model-based a priori variance in regions where the models have insufficient data, followed by the generation of a “time-correlated” solution that uses statistical information on mass variability from the white noise solution to derive better optimized constraints. These two processes are described in detail below.

#### 4.1. Step 1: Development of a White Noise Solution

The first step in our process involves the application of a geophysically realistic  $\bar{P}_0$  matrix (see below) while specifying  $\bar{x}_0 = 0$  (that is, we do not use the a priori value of the model-based mass flux, but only the variance;



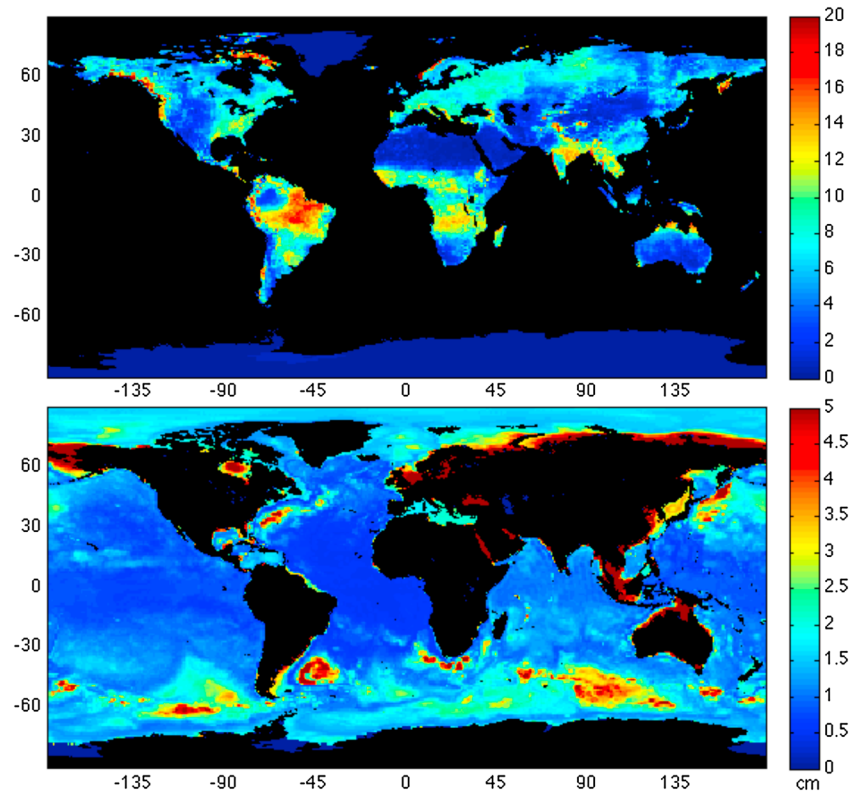


**Figure 4.** (top) Monthly mean RMS of GLDAS-NOAH terrestrial water storage from 2003 to 2010 and the (bottom) maximum of the monthly mean RMS of the ECCO2 and (ECCO2-OMCT) model ocean bottom pressure from 2004 to 2007 (bottom). Units are in centimeter of equivalent water height.

hence, we refer to this as a white noise approach). We perform this step because forward models of mass variations over ice-covered regions are presently not fully reliable, and the hydrological models are also likely to be in error in certain regional areas. Thus, a bootstrapping methodology is implemented to derive appropriate a priori values for variability. This approach is designed to minimize striping in the solutions while maximizing the retention of geophysical signals. The a priori uncertainties in  $\bar{P}_0$  for each individual mascon  $\sigma_i^A$  are chosen to be

$$\sigma_i^A = W_j^A \text{RMS}_i^k \sqrt{\cos \varphi_i}, \quad i = 1, \dots, 4551. \quad (15)$$

In equation (15),  $W_j^A$  is an empirically determined weighting factor on the a priori covariance for each month,  $j$ , tailored to complement the weights on the KBR information equations, while  $\varphi_i$  is the latitude of the center point of mascon  $i$ . The latitude dependence is introduced to compensate for more frequent ground track crossings (and thus more accurately determined mascons) at higher latitudes.  $\text{RMS}_i^k$  is the RMS of a monthly averaged time series of a geophysical model representing mass variations in mascon  $i$ , bounded within region  $k$ . We define six specific regions  $k$

$$k = \left\{ \begin{array}{l} \text{Land}(L), \\ \text{Ocean}(O), \\ \text{Ice}(I), \\ \text{Inland Seas}(IS), \\ \text{Earthquake}(EQ), \\ \text{Glacial Isostatic Adjustment (GIA)} \end{array} \right\}. \quad (16)$$

$\text{RMS}_i^L$  is derived from monthly averages of the Global Land Data Assimilation System (GLDAS)–NOAH model [Rodell *et al.*, 2004] from 2003 to 2010, shown in Figure 4 (top). As can be inferred from Figure 4, mascons in

the Amazon River Basin, where variability is high, are given a larger a priori uncertainty than mascons in the Sahara desert, where variability is expected to be low.  $RMS_i^O$ , on the other hand, is not as straightforward to calculate since OMCT is modeled as a background model during the data processing [Flechtner, 2007]. Here it is assumed that the difference between two ocean models represents a realistic estimate of the uncertainty of the ocean background model. Therefore,  $RMS_i^O$  is derived from the difference between monthly averages of the Estimating the Circulation and Climate of the Ocean Phase 2 (ECCO2) [Menemenlis et al., 2008] and OMCT ocean models from 2004 to 2007. However, if for any mascon the RMS of ECCO2 exceeds that of (ECCO2-OMCT), then  $RMS_i^O$  is set equal to the RMS of ECCO2. This substitution is performed in an effort not to overconstrain the solution in areas where perhaps the two models agree but are both incorrect. Figure 4 (bottom) shows the greater of the RMS values obtained from ECCO2 or (ECCO2-OMCT), and is used to calculate  $RMS_i^O$ .

We define ice-covered regions to be Greenland, Antarctica, Alaska, Patagonia, Baffin Island, Ellesmere Island, and Iceland. While there are other regions of the world that are glaciated (Svalbard, Scandinavia, Himalayas, etc.), constraints derived from GLDAS proved to be adequate for recovering mass variations in these regions, predominately because the ice signal is small [Jacob et al., 2012] relative to the regions we define as ice. Our methodology to derive the constraints in ice-covered regions consists of first solving for mass variations with extremely loose constraints over the entire GRACE time span. The resulting time series over the ice-covered regions is noisy but succeeds in deterministically localizing areas of strong signal versus areas of weak signal spatially. We then derive the final  $RMS_i^I$  values by taking the maximum deviation from the static field for each mascon from this solution, and using this for  $RMS_i^I$ . The result is a spatially varying a priori covariance matrix over ice-covered regions for which the spatial variance is dictated by the KBR data.

Other regions of the world for which models are not available to derive a priori information are inland seas, or large inland lakes, such as the Caspian Sea. In total, we identify 20 such large bodies of water. For these regions, altimetry data from Crétaux et al. [2011] are used to derive  $RMS_i^S$  by calculating the RMS of the altimetry solution over the time span of the GRACE data. Since the altimetry signal consists of both a steric and nonsteric (mass) component, and GRACE is only sensitive to the nonsteric component, the derived constraints are considered to be conservative.

Special consideration must also be given to regions that have been affected by earthquakes large enough for GRACE to be sensitive to. In particular, the 2004 earthquake in Sumatra, the 2010 earthquake in Chile, the 2011 earthquake in Japan, and the 2012 earthquake in the Indian Ocean were all large enough to be detected by GRACE. To allow for the full recovery of these earthquakes, the a priori variance in these regions must be increased to reflect the expected mass changes due to the earthquake. We use models for these earthquakes given by Han et al. [2013] to derive  $RMS_i^{EQ}$ . The a priori covariance matrix is modified as a step function when the earthquakes occur, by adding  $RMS_i^{EQ}$  to the existing  $RMS_i^k$  values.

Finally, glacial isostatic adjustment (GIA) signals must be considered when developing  $\bar{P}_0$ . We derive  $RMS_i^{GIA}$  from the Paulson model [Paulson et al., 2007] that uses ICE-5G [Peltier, 2004] for loading history. This model is again considered to be conservative, particularly for Antarctica where a new generation of models shows the GIA correction to be considerably smaller [Ivins et al., 2013]. Similar to the earthquake constraints,  $RMS_i^{GIA}$  is added to existing  $RMS_i^k$  values since total mass flux must be considered when developing  $\bar{P}_0$ . The magnitude of  $RMS_i^{GIA}$  is based on the largest time offset ( $\sim 7$  years for data through the end of 2013) from the epoch of the background static gravity field model.

Once all  $RMS_i^k$  values are derived, the  $\bar{P}_0$  matrix is specified in equation (13), and the white noise monthly gravity field solutions are estimated and subsequently used to derive the monthly a priori variance used in the second time-correlated final solution. The primary advantage of implementing time correlation is that it allows the filter to account for gross unresolved geophysical processes in the models, particularly trends. The white noise monthly solutions have a difficult time capturing these unresolved processes unless the a priori monthly variance is unnaturally inflated, which is undesirable as it results in solutions with larger noise in these regions.

## 4.2. Step 2: Development of a Time-Correlated Solution

Some existing harmonics solutions [Kurtenbach et al., 2009] and mascon solutions [Luthcke et al., 2013] have demonstrated the successful implementation of time correlation in their solution processes. In our approach,

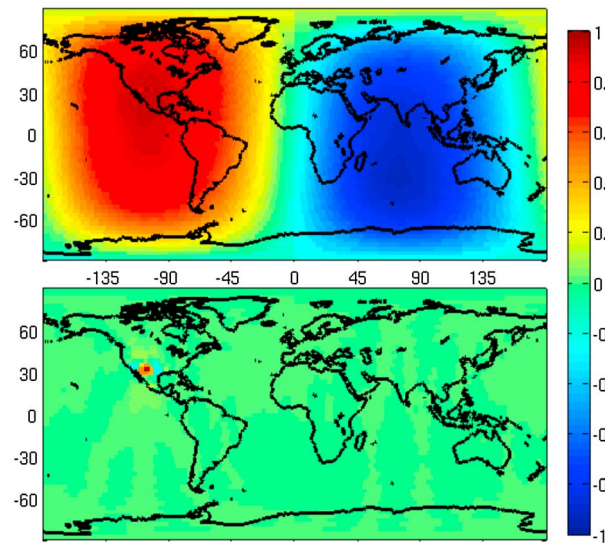


**Figure 5.** Posteriori correlation coefficient of a mascon in the southwest United States with all other mascons (top) when a priori correlation is zero and (bottom) when a priori correlation is introduced via GLDAS correlations.

we introduce time correlation via the specification of a nonzero  $\bar{x}_0$  in equation (13). In this process, the a priori estimate of the state for a given month  $i$  is prescribed to be the estimated mascon value of the previous month  $i - 1$ , as reflected in equation (17).

$$\bar{x}_0^i = \bar{x}_0^{i-1} \quad (17)$$

Furthermore,  $\bar{P}_0$  for a given month,  $i$ , is now specified to be the posteriori covariance ( $P$ ) of the previous month plus some specified process noise ( $\delta$ ), as seen in equation (18). This process is essentially the implementation of a sequential Kalman filter for the monthly solutions.

$$\bar{P}_0^i = P^{i-1} + \delta. \quad (18)$$

The process noise in equation (18) is chosen such that it reflects the estimated month-to-month variability of each mascon in the white noise solution from Step 1. As

such, mascons in the Amazon River Basin have a larger process noise component than mascons in the Sahara Desert, for instance. We implement this time correlation procedure going forward and backward in time, initiating the filter at the epochs with white noise constraints as derived in section 4.1, and then taking the optimal combination (including covariance information) of these two solutions to get the final answer. During this process, all ocean mascons are solved for via methods described in section 4.1; that is, they are specified to have an a priori estimate ( $\bar{x}_0$ ) equivalent to zero. Since we do not expect large trends in the ocean, and the constraint system described in section 4.1 was found to be adequate for determining ocean signals, it was deemed undesirable to specify time correlation for these mascons.

### 4.3. A Priori Spatial Correlations

In addition to the diagonal constraints described above, we also introduce an off-diagonal a priori correlation between mascons ( $\rho_{ij}$  in equation (14)) in cases where it can be reliably established. Figure 5 (top) shows the posteriori correlation of a particular mascon in the southwest United States with all other mascons globally in a completely unconstrained case for which no a priori correlation is introduced. It is seen that in the unconstrained case, this particular mascon is positively correlated with other mascons in a large surrounding area and is negatively correlated with mascons on the other side of the Earth. This indicates that the filter cannot independently distinguish which mascon is causing the particular acceleration that the spacecraft are experiencing. This is akin to unconstrained harmonic solutions, which show posteriori correlations between coefficients of a fixed order and the same parity of degree. For harmonics, these correlations can be empirically removed in a postprocessing step by applying a destriping filter [Swenson and Wahr, 2006].

In our solution, the a priori spatial correlation is introduced in equation (14) via empirically calculating the correlations using the same models we use in setting the diagonal terms. We assemble the GLDAS and ECCO2 models together to gather a global map of mass variations (with the exception of ice-covered areas). Note that altimetry data are also added to this map to reflect mass changes over the inland seas. This time series of mass variations is then “mascon averaged” and correlations between nearby mascons (within a 750 km radius for ocean areas and a 500 km radius for land areas) are calculated to obtain the  $\rho_{ij}$  values in equation (14). We set the a priori correlations to zero for any mascons separated by more than 750 km in the ocean and 500 km over land. Since the correlation matrix must be symmetric and positive definite, we solve for the nearest correlation matrix [Higham, 2002] using the technique outlined in Qi and Sun [2006] to gain the final values for  $\rho_{ij}$ . Solving for correlations in this manner allows for “automatic” global distinction of general oceanic and hydrologic basin boundaries, as opposed to fixed boundaries which are potentially erroneous or

which vary slightly over time. Since we lack reliable models for the ice-covered regions, we conservatively specify zero a priori correlation in these regions. Additionally, a hard constraint is imposed to dictate zero a priori correlation between land and ocean areas. Mascons that span land/ocean boundaries are assigned as either “land” or “ocean” dependent on if the particular mascon has a higher correlation to adjacent land or ocean mascons. Furthermore, a priori spatial correlations for earthquake regions are derived via the earthquake models and are included as a step function in the a priori covariance matrix when the earthquake occurs.

Figure 5 (bottom) shows the posteriori correlations for the same mascon in the southwest United States after introducing a priori spatial correlations via the models. As can be seen, the posteriori correlations are reduced substantially over the unconstrained case. Some residual posteriori correlations with a magnitude of approximately 0.4 remain in adjacent mascons, indicating that the data are not strong enough to perfectly determine white noise  $3^\circ$  mascons at this latitude. Note that these off-diagonal constraints are implemented in both the white noise and time-correlated solutions, and are consistent between the two.

The quality of the final JPL RL05M solution is presented in section 7, where global and regional comparisons for ocean, hydrology, and cryosphere are made with the current state-of-the-art spherical harmonic solutions and OBP sensors.

## 5. Scale Factors for Mascon Solutions

One subject that deserves attention is the interaction of spherical cap mascons versus traditional unconstrained spherical harmonics with the posteriori scaling often used to correct for amplitude changes due to spatial averaging. This scaling is typically done on the solutions to better account for actual mass lost (or gained) after destriping and smoothing. For instance, when destriping a gravity field via *Swenson and Wahr* [2006], an undesired effect of applying this filter is the removal of mass from the solution, particularly in regions oriented in the north-south direction. Derived scale factors can then be applied to the solution to account for this lost mass, albeit with some regional and timescale dependent limitations [*Landerer and Swenson*, 2012]. The advantage to having constrained mascon solutions is they do not require the user to apply any postprocessing filters to the data, as most correlated (stripe) noise has already been removed through the introduction of the a priori information. However, having equal-area  $3^\circ \times 3^\circ$  mascons as basis functions imply an inherent smoothing function on the data. Thus, scale factors should still be derived for the mascon solutions based purely on how this  $3^\circ$  averaging affects the solution. The most straightforward way to derive these scale factors for land areas is to spatially average the  $1^\circ \times 1^\circ$  GLDAS monthly averaged time series into equal-area  $3^\circ$  bins, consistent with the mascon placement in the gravity solution. A least squares fit is then performed between the  $1^\circ \times 1^\circ$  GLDAS product and the equal-area  $3^\circ \times 3^\circ$  GLDAS product to fit a scale factor for each  $1^\circ \times 1^\circ$  bin. Similar scale factors can be calculated for harmonic solutions due to selected postprocessing procedures [*Landerer and Swenson*, 2012]. Figure 6 compares the derived scale factors for harmonics (top) and mascons (bottom) by using the GLDAS model time series from 2003 to 2012. Note that the harmonic scale factors are derived from truncation at degree 60, destriping via *Swenson and Wahr* [2006], and smoothing the solutions with a 300 km averaging radius. The mascon scale factors are derived from the equal-area  $3^\circ \times 3^\circ$  spatial averaging that occurs during the estimation process.

The scale factors for the mascon solutions are substantially smaller than those associated with the postprocessed spherical harmonic solutions (Figure 6). This result demonstrates a significant advantage for using mascon solutions since there are substantial uncertainties with the derived spherical harmonic scale factors [*Landerer and Swenson*, 2012]. The smaller mascon gain factors reduce any dependence of mass flux estimates on the scaling. Further information can be found in *Wiese et al.* [2013].

## 6. Reducing Leakage Errors in Mascon Solutions

Another source of error in the GRACE solutions comes from leakage; i.e., mixing of signals on land into the ocean and vice-versa. Leakage errors are inherent in the spherical harmonic GRACE solutions due to the modest spatial resolution of the derived gravity products (truncation at degree 60) coupled with the necessity to smooth the solutions to damp high-degree errors. Leakage errors are introduced in the mascon solutions when a single mascon is placed over both land and ocean areas. The filter solves for the average mass over the particular mascon and does not discriminate between land and ocean boundaries within the mascon. Figure 7 shows the global placement of mascons and discriminates between mascons that cover purely land areas (L),



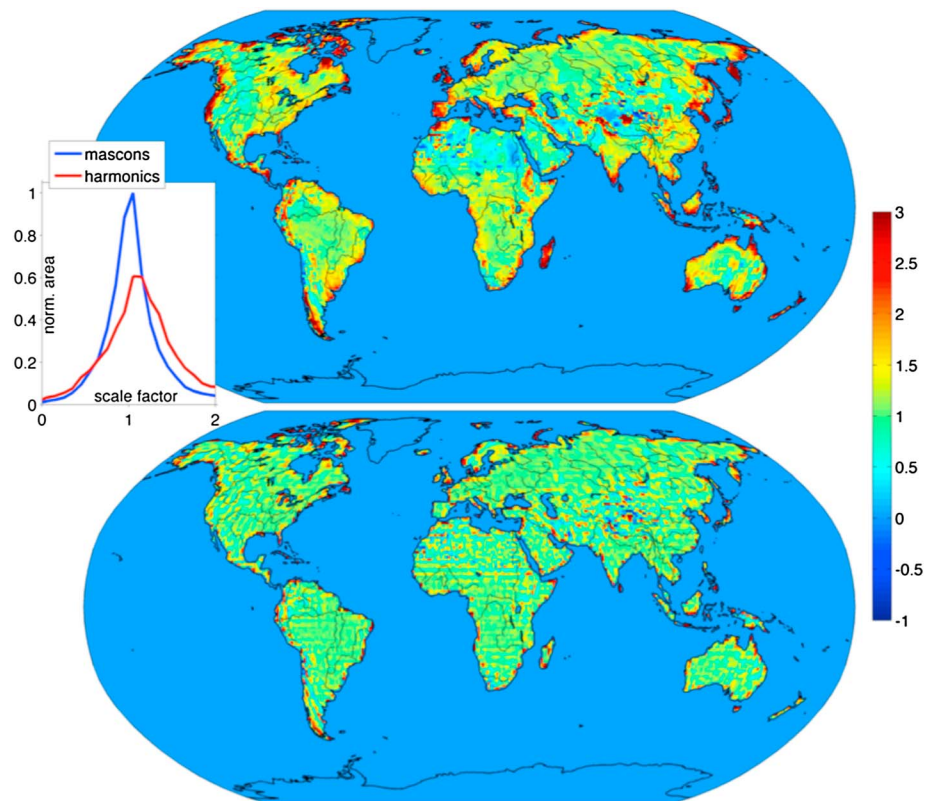


**Figure 6.** Scale factors calculated on a  $1^\circ \times 1^\circ$  grid for (top) spherical harmonic solutions due to destriping, truncation at  $n = 60$ , and smoothing at 300 km, and (bottom) mascon solutions from  $3^\circ$  equal-area spatial averaging. The histogram (inset) of the scale factors reveals that the mascon approach yields significantly more scale factors closer to one.

purely ocean areas (O), and which mascons are over both land and ocean areas (L/O). In all, 796 of the 4551 mascons are classified as L/O mascons. Each of these L/O mascons contributes leakage error to the solution when calculating basin averages containing those particular mascons.

To reduce the leakage error inherent in the mascon solutions, we developed an algorithm to redistribute mass within a L/O mascon independently to the land and ocean portions of the particular mascon. This redistribution is performed by solving the observation equation

$$A_T M_T = A_L M_L + A_O M_O \quad (19)$$

using least squares, where the observation  $M_T$  is the total mass of the mascon in question, and the state parameters to be estimated are,  $M_L$ , the mass over the land portion of the mascon, and  $M_O$  the mass over the

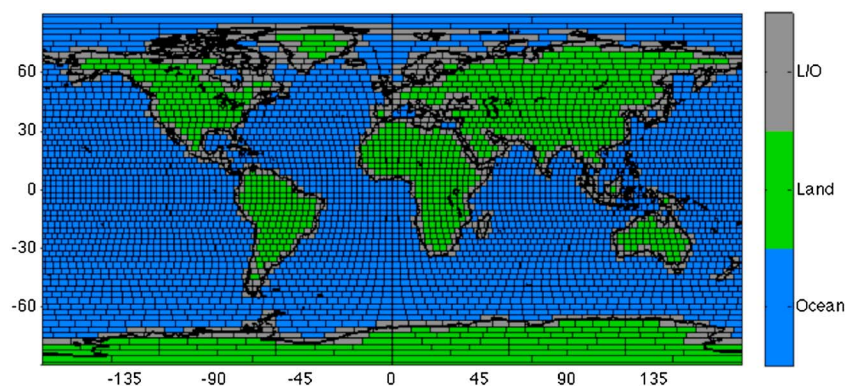


**Figure 7.** Definition of land, ocean, and land/ocean mascons.



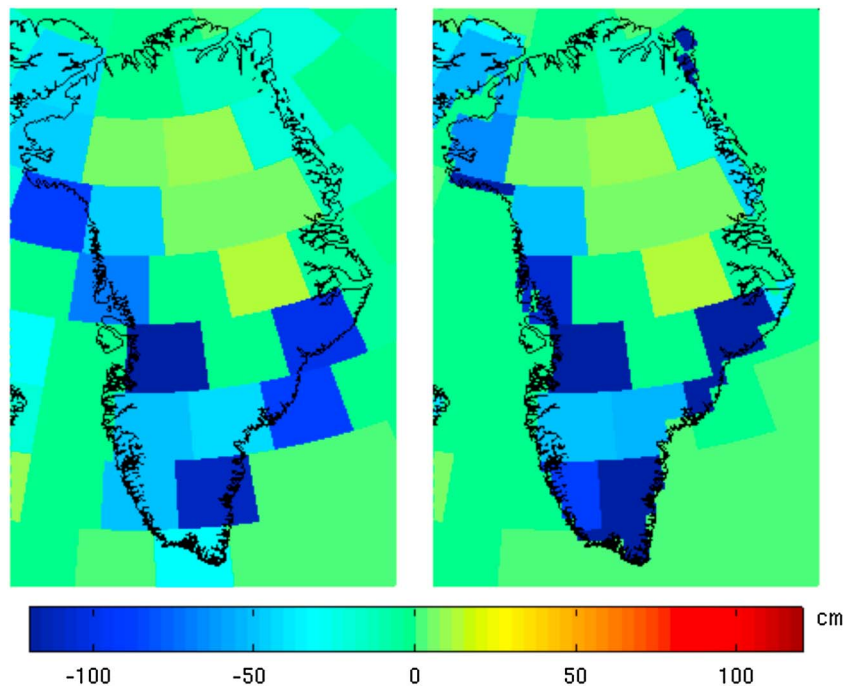


**Figure 8.** Mascon mass anomalies expressed on a grid for April 2011 in centimeter of EWH (left) before and (right) after correcting for leakage errors due to mascon placement over land/ocean boundaries.

ocean portion of the mascon, with each “mass” term being expressed in centimeter of equivalent water height.  $A_T$  is the total area of the mascon, and  $A_L$  and  $A_O$  are the areas of the land and ocean portions of the mascon, respectively. This system is underdetermined, given the fact that the number of state parameters exceeds the number of observations. However, we add a priori information to the system to enable a solution. A priori estimates for the state parameters ( $\bar{x}$ ) are calculated by taking the average mass of adjacent mascons of the same type (land or ocean). We also provide variance information on the state ( $\bar{P}_o$ ) derived from models by calculating the standard deviation between two time series: the average mass of the land or ocean part of the mascon in question and the average mass of adjacent land or ocean mascons used to calculate  $\bar{x}$ . Hence, the filter relies on an a priori estimate of the land and ocean parts of the mascon derived from estimated values of adjacent mascons, along with uncertainty information on these a priori estimates that have been derived from models to then redistribute mass across land/ocean boundaries. Note that the observation is weighted heavily to conserve the total mass of the mascon during this process. This is an iterative process since values for  $\bar{x}$  and  $\bar{P}_o$  are not available for all L/O mascons during the first iteration. After reassigning mass to land and ocean areas during the first iteration, these values can then be used to calculate  $\bar{x}$  and  $\bar{P}_o$  in subsequent iterations. Simulation results showed that our algorithm reduces leakage errors more than 50% globally.

Correcting for leakage errors is extremely important when calculating mass balances for regions on land/ocean boundaries. For example, Figure 7 shows that the majority of the mascons over Greenland are classified as L/O mascons, and estimates of ice mass loss are therefore sensitive to this redistribution of mass. This effect can be seen in Figure 8, where mass anomalies are shown for April 2011, expressed in centimeter of equivalent water height (EWH). Figure 8 (left) shows the “raw” mascon solution. Several mascons lie on land/ocean boundaries, and much of the mass loss from Greenland is being leaked into the ocean. After redistributing the mass by solving equation (19), most of the mass signal over the ocean is now placed over land (Figure 8, right). This effect changes the trend in Greenland by as much as 15% when using an exact averaging kernel, which arises because much of the ice mass loss is concentrated along the coastal regions [Schrama and Wouters, 2011]. The redistribution process via equation (19) can be thought of as being a more rigorous analog of extending an averaging kernel into the oceans when calculating mass loss from Greenland with spherical harmonics to account for leakage errors [Baur et al., 2009; Velicogna, 2009]. Further information on this process can be found in Wiese et al. [2013].

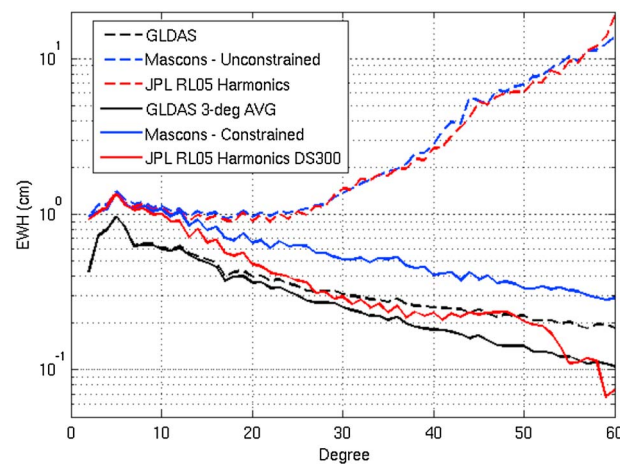


**Figure 9.** Degree variance of the GLDAS model compared with unconstrained harmonic and mascon solutions, and 3°-averaged GLDAS compared with constrained mascons and harmonics that have been destriped and smoothed with a 300 km averaging radius.

### 7.1. Global Comparisons

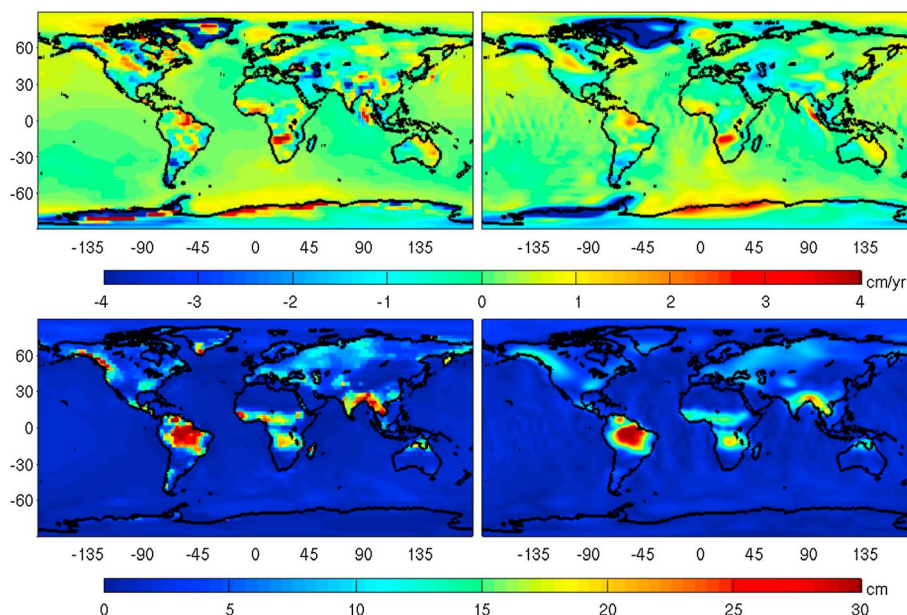
Figure 9 compares the power in GLDAS with that of unconstrained JPL RL05 harmonics and mascons. Note that the unconstrained mascon solution is obtained by inverting for the gravity solution without the addition of  $\bar{P}_0$ . The power is obtained by averaging over each monthly solution from January 2004 to December 2010 and zeroing out all ocean and ice areas to make a fair comparison with GLDAS. Without constraints, the mascons and harmonics have similar amounts of power (as expected), and in both solutions the power greatly exceeds that of GLDAS. This result is consistent with the mascon solutions produced by Goddard Space Flight Center [Rowlands *et al.*, 2010] and reinforces the concept that simply using mascons as a basis function does not inherently provide an advantage in obtaining a more accurate gravity solution. The advantage comes in the convenience the basis function allows for implementing an optimal a priori covariance matrix.

Figure 9 additionally compares the power in the GLDAS model after it has been averaged over equal-area  $3^\circ \times 3^\circ$  bins with the same mascon placement as in the mascon solution, along with the JPL RL05M constrained mascon solution and JPL RL05 harmonics that have been destriped via Swenson and Wahr [2006] and smoothed with a 300 km averaging radius (DS300). The reason for  $3^\circ$  averaging GLDAS is that, in theory, if  $1^\circ \times 1^\circ$  GLDAS represented the true mass variations over land areas,  $3^\circ$  averaging this product would represent the best solution that one could obtain given the mascons as a basis function. Note that when comparing the two GLDAS curves in Figure 9, it is seen that this averaging has the effect of damping the power in GLDAS at high degrees; it is for this reason that scale factors should be applied to the solutions, as discussed in section 5. It is seen that both the constrained mascon solution and postprocessed harmonic solution agree well with GLDAS, although there is slightly more power in the mascon solutions than in the postprocessed harmonics, presumably in large part due to the spherical harmonic postprocessing methods removing real geophysical signals which the mascon solutions retain. The power in the mascon solution is seen to exceed that of GLDAS at all wavelengths, which is expected, as GLDAS does not account for surface water nor ground water past 2 m depth, both of which GRACE is sensitive to. Figure 9 does not directly compare the solutions after scale factors have been applied; however, the effect of applying scale factors to hydrology signals is discussed in section 7.2.2.

For another global comparison, the trends and annual amplitudes between JPL RL05M mascons and JPL RL05 harmonics are compared against one another. The trends from land ice melting [Velicogna, 2009; Schrama and Wouters, 2011] and groundwater depletion [Famiglietti *et al.*, 2011; Rodell *et al.*, 2009; Tiwari *et al.*, 2009] are of particular interest, as these signals are primarily associated with both natural and anthropogenic secular change. The majority of the large trend signals are similar between the JPL RL05M mascons (Figure 10, left) and JPL RL05 harmonics DS300 (Figure 10, right), although there is better apparent resolution in the mascon trend map, as evidenced by small-scale signals in South America and Asia. The drought signal in the

## 7. Solution Comparisons: Mascons Versus Spherical Harmonics

In this section, we perform both global and regional comparisons of the mascon solutions to state-of-the-art spherical harmonic solutions and in situ data where available. All data have been processed such that the  $C_{20}$  coefficients have been replaced with an SLR-derived value [Cheng and Tapley, 2004], degree 1 terms have been calculated according to Swenson *et al.* [2008], and glacial isostatic adjustment (GIA) signals have been removed using the Paulson model [Paulson *et al.*, 2007] with ICE-5G [Peltier, 2004] for loading history and a viscosity profile adjusted to match the GRACE observations, unless otherwise mentioned.



**Figure 10.** The 2003–2013 (top) trend and (bottom) annual amplitude for (left) JPL RL05M mascons and (right) JPL RL05 harmonics DS300 expressed in cm/yr and centimeter of EWH, respectively. Color scale has been intentionally saturated.

South central United States is much more prominent in the mascon trend map than the harmonics. Additionally, one can see how the mass loss signal from Greenland is spread out over a large area in the harmonic solution but is concentrated within the boundaries of Greenland in the mascon solution especially after correcting for leakage errors from L/O mascons.

Figure 10 additionally compares the annual amplitudes (bottom) between JPL RL05M mascons (left) and JPL RL05 harmonics DS300 (right). Similar to the trend map, the large signals qualitatively agree with one another; however, the signal magnitudes of the mascon solution slightly exceed those of the harmonic solution. The annual amplitudes in southern Greenland, along the northwestern coast of North America, the southwestern coast of South America, and over Africa and India are much more prominent in the mascon solution than the harmonic solution.

## 7.2. Regional Comparisons

### 7.2.1. Oceans

Over the ocean, GRACE gravity observations are equivalent to ocean bottom pressure (OBP) signals on spatial scales of approximately 300 km. In situ OBP data from bottom pressure gages provide a means to evaluate the ability of GRACE to capture oceanic signals. A number of studies have shown that GRACE is able to observe signals measured by the OBP sensors to a significant extent [Kanzow *et al.*, 2009; Rietbroek *et al.*, 2006; Park *et al.*, 2008; Böning, 2009; Macrander *et al.*, 2010; Morison *et al.*, 2007]. Best agreement is usually found in large-scale ocean circulation regimes where the spatial coherence is high [Böning *et al.*, 2008]. However, high small-scale variability related to eddy activity in many regions dominates the pointwise in situ measurements and complicates comparison to GRACE observations which represent signals at a spatial resolution of a few hundred kilometers [Park *et al.*, 2008].

In the framework of a project to validate GRACE OBP started in 2005 at the Alfred Wegener Institute for Polar and Marine Research, all available OBP records concurrent with the GRACE operation period 2002 to present were entered into a database [Macrander *et al.*, 2010]. At present, the database contains time series from 105 deployments at 74 different locations of predominantly 1 year duration. All data were quality controlled. Outliers, predeployment values, and pressure jumps were removed. A common problem of pressure sensors is their long-term drift, with larger drift rates during the first weeks to months of the deployment and smaller drift rates later on. The nonlinear drift characteristic prohibits a linear interpolation between predeployment and postdeployment calibrations (if these are available at all). Therefore, sensor drift was eliminated by an empirical exponential linear least squares fit. Thus, the in situ data cannot be used to evaluate OBP trends.

To establish a statistically meaningful assessment, several conditional constraints were applied to select high quality in situ time series for the comparison to GRACE data. As a first step, records from subsequently deployed bottom pressure recorders (BPRs) were merged to one long time series at each respective location. Time series covering a period shorter than 2 years or containing gaps of longer than 1 month were omitted from the comparison. Regions with high small-scale variability due to eddy activity (as in part of the Kuroshio Extension System Study array) were left out as well, since variability on these scales cannot be captured by GRACE [Park *et al.*, 2008]. In total, this leaves 16 in situ OBP time series for the comparison. The BPR arrays are located in the Arctic Ocean, North, tropical and South Atlantic, and the Kuroshio Extension in the Northwest Pacific, respectively (Figure 11).

To evaluate the quality of our solutions, we calculate correlations between in situ OBP in these five regions of the ocean (Figure 11) with JPL RL05M mascons, JPL RL05 harmonics, and CSR RL05 harmonics, which is the solution from the Center for Space Research (CSR). Correlations between GRACE and in situ data are positive and mostly higher than 0.5, which indicates the overall ability of GRACE to capture oceanic variability at the scales represented by the in situ measurements. In general, the unsmoothed JPL RL05M mascon solution exhibits comparable and often slightly higher correlations than the JPL RL05 and CSR RL05 spherical harmonic solutions (after both destriping and smoothing at 500 km) with most of the in situ time series. In the Kuroshio Extension (region E)—a strong western boundary current—where temporal and spatial variability is high, the correlation between in situ and GRACE-derived OBP ranges between 0.5 and 0.8 for both the mascon and harmonic solutions. Thus, in general, oceanic variability is captured well by the satellite measurements. However, it is worth noting that nonmesoscale variability in the Kuroshio is already well modeled by the background ocean model OMCT.

With the mascon solution, significant progress has particularly been achieved in low-latitude regions (region B). In the tropical Atlantic where the signal-to-noise ratio (SNR) is low, the mascons account for a significant part of the oceanic variability observed by the BPRs (Figure 11). While barotropic dynamics are weak, leading to a low-amplitude OBP signal, this area is additionally affected by hydrologic leakage from the close-by Amazon River basin compromising the OBP data derived from spherical harmonic solutions. Therefore, it has previously been difficult to capture the small oceanic signal in the GRACE solutions [Kanzow *et al.*, 2009; Böning, 2009]. While the JPL and CSR RL05 spherical harmonics still lack agreement with the in situ data, the mascon approach clearly captures variability in the tropical Atlantic. Note that whereas the constraints in this region are particularly strong (Figure 4), the reason for the agreement is not related to an initially good agreement with the background ocean model. On the contrary, OMCT fails to reproduce the low-amplitude signal and exhibits correlations less than 0.3 (Figure 11) to the in situ data.

This demonstrates that not only in regions with high SNR, for example, at high latitudes (Arctic and Southern Oceans), the mascon solution captures oceanic signals well, but it also exhibits significant skill in capturing variability in low-latitude regions. Furthermore, it should be noted that the mascon solution has a lower error RMS than the harmonics with respect to the OBP data (Figure 11) for all 16 BPRs (with the exception of two BPRs in region C for which CSR harmonics have slightly lower RMS values), on average reducing the error RMS by 0.35 cm. In the low-latitude oceans (region B), the error RMS is reduced by more than 1 cm for one of the BPRs and more than 0.4 cm for the other. Hence, the mascon solution constitutes the first GRACE data product that has the potential to enable future studies of the low-latitude oceans.

### 7.2.2. Hydrology

The 50 largest hydrological basins in the world are analyzed for the time period 2003–2012, comparing JPL RL05M mascon solutions, JPL RL05 harmonics (after destriping and smoothing with a 300 km radius), and the GLDAS model. The effect of applying scale factors to the mascon and harmonic solutions is also analyzed, as discussed in section 5. Basin averages for all 50 basins are computed, and a simultaneous fit of an annual, semiannual, trend, bias, and 161 day period S2 tidal alias term are made to the time series. Figure 12 shows the annual amplitude part of this fit comparing the mascons to both the harmonics (filled circles) and the GLDAS model (open circles), both with scale factors applied (right) and without scale factors applied (left). Note that the basins are color coded by area, and the logarithmic scale reflects the area of the basin. If the mascon and harmonic solutions agreed perfectly, the filled circles would align on the  $y = x$  axis (black line), and a line could be fit through them with a slope of identically one.

The results show that prior to adding scale factors (Figure 12, left), the mascon solution has significantly more power than the harmonic solution, as evidenced by the fact there are more data points below the  $y = x$  axis



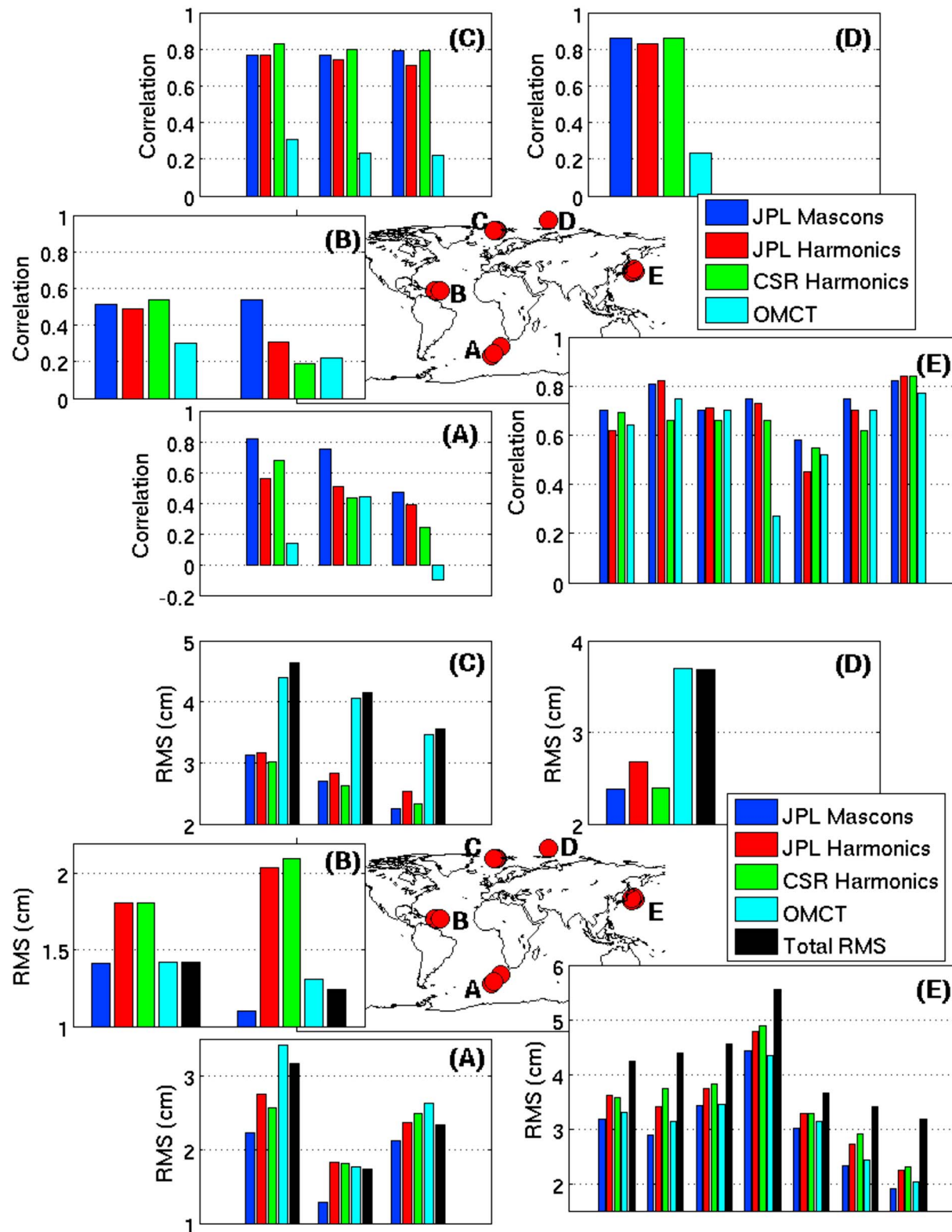


**Figure 11.** (top) Correlations of 16 in situ BPRs with JPL RL05M mascons, JPL RL05 harmonics, CSR RL05 harmonics, and OMCT, and (bottom) error RMS of each solution with respect to the in situ BPR data.



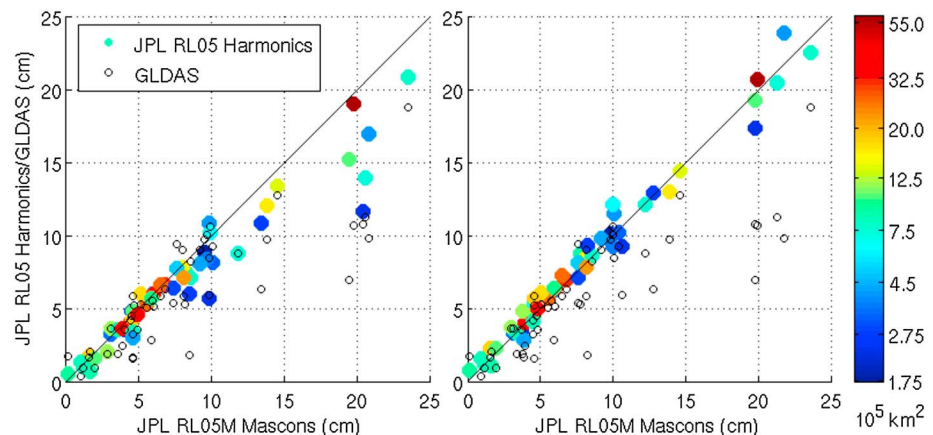


**Figure 12.** Scatterplot of annual amplitudes for 50 river basins comparing JPL RL05M mascons (abscissa) to both JPL RL05 harmonics (filled circles; ordinate) and GLDAS (open circles; ordinate) for the time period 2003–2012 (left) without scale factors and (right) with scale factors applied. Basins are color coded by area, and the logarithmic scale of the colorbar reflects the basin area.

than above it. Further analysis shows that the most significant differences show up in small basins with large annual amplitudes. Similarly, the mascon solution has significantly more power than the GLDAS model, confirming the result shown in Figure 9. It is important to note that even though the variance of the GLDAS model is used to derive the a priori covariance matrix, the looseness of the applied constraint coupled with the implementation of time correlation allows for significant deviations from the model variance to be estimated and follow the GRACE data, as desired.

After scale factors are applied to both the mascon and harmonic solutions (Figure 12, right), the two solutions agree much better. The RMS about the  $y=x$  axis is reduced from 1.48 cm to 0.60 cm with the addition of the scale factors, and there is no discernible pattern in basin size or amplitude that the results are skewed toward. This level of agreement between the two solutions demonstrates both the skill of the mascon solution as well as the skill in postprocessing the harmonic solution and the derivation of the associated scale factors. Furthermore, the results in Figure 12 (right) imply that GLDAS can accurately capture the spatial patterns of mass changes because the derived scale factors are accurate to the level that the mass balances between the harmonic and mascon GRACE solutions agree.

Additionally, we note that applying the scale factors changes the harmonics solution substantially more than the mascon solution, as indicated in Figure 6. We calculate the percentage change in the annual amplitude for all 50 basins that is obtained by applying the scale factors. The RMS of the percentage change for all 50 basins is 7% for the mascon solutions versus 31% for the harmonic solutions.

The application of scale factors is suitable for studying seasonal and subseasonal timescales, and Figure 12 shows good agreement between the harmonic and mascon solutions after scale factors are applied. However, the scale factors are not as well suited for resolving longer period surface mass changes because these signals are not well represented in the synthetic model used to generate the scale factors [Landerer and Swenson, 2012]. Therefore, the reduced amplitudes and dependencies on empirically derived scale factors provide a clear advantage for the mascon solution. As an example of this, the 2003–2013 trends of total terrestrial water storage over the United States determined from the mascon solution enable a significant improvement in localizing the drought signals in California [Famiglietti et al., 2011] and Texas [Long et al., 2013] compared to the conventional harmonic solution (Figure 13). The mascon data could thus further enhance products that assimilate GRACE data, such as the United States Drought Monitor [Houborg et al., 2012].

### 7.2.3. Cryosphere

A large number of studies have used GRACE data to calculate mass loss rates from the Greenland and Antarctic ice sheets. The majority of those studies have used spherical harmonic solutions to calculate mass changes, with the exception of a few which have used a type of mascon solution [Luthcke et al., 2013]. The studies that use spherical harmonic solutions vary substantially in the way they treat the GRACE observations.

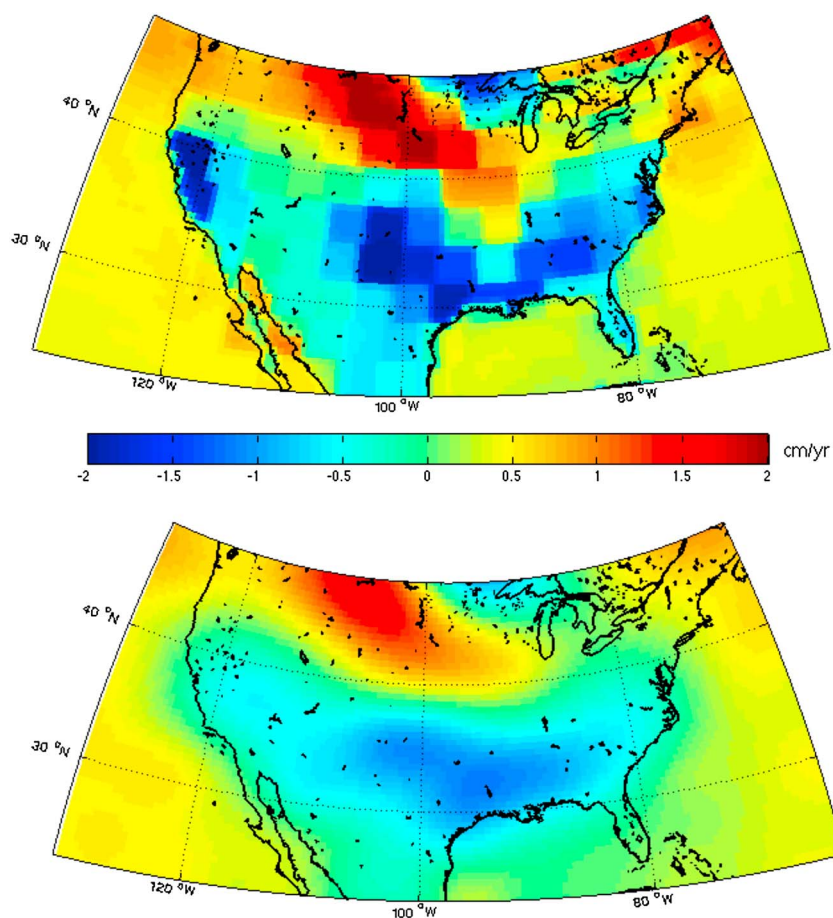


**Figure 13.** The 2003–2013 trends for the United States comparing the (top) JPL RL05M mascon solution and (bottom) JPL RL05 spherical harmonic solution DS300.

An array of postprocessing techniques has been deployed on the gravity solutions to remove and smooth through correlated errors, including empirical orthogonal function filtering [Schrama and Wouters, 2011], Wiener optimal filtering [Sasgen et al., 2012], and destriping and Gaussian smoothing [Baur et al., 2009; Chen et al., 2011]. A variety of techniques have also been used to subsequently calculate mass loss rates, including applying optimal averaging kernels with scale factors [Velicogna, 2009], fitting harmonics to regional mascons [Jacob et al., 2012], fitting harmonics to a forward model for Greenland basins [Schrama and Wouters, 2011; Chen et al., 2011], and simultaneously estimating glacial isostatic adjustment (GIA) and gravity anomalies using both GRACE data and GPS measurements of uplift [Ivins et al., 2011]. There are also various models one can apply to correct for GIA, and each study handles this somewhat differently. Typically, however, the GIA correction for Greenland amounts to changes in the trend of less than 10 GT/yr while the GIA correction in Antarctica is much larger, ranging from approximately 55 GT/yr with the new IJ05\_R2 model [Ivins et al., 2013] to 141 GT/yr with the outdated ICE5G [Peltier, 2004] loading history model. Each of these differences, along with others that have not been mentioned here, leads to discrepancies in overall estimates for how much mass the ice sheets are losing.

Table 4 lists some of the more recent studies and their published estimates of the rate of ice mass loss from Greenland and Antarctica, and compares the published trends with the trend we derive using the JPL RL05M mascons for the same time frames. Since the main purpose of Table 4 is to compare various mass balance estimates as computed using different techniques, we omit the GIA correction for Antarctica (since this is rather large, and estimates vary considerably from study to study), but we do include the GIA correction for Greenland (since the correction is rather small). JPL RL05 harmonics are omitted from this comparison since many published estimates of ice mass loss derived from harmonics are already available. We correct for leakage effects on land/ocean boundaries (see section 6), and the GIA correction for Greenland is based on

**Table 4.** Comparison of Published Trends for Greenland (Including GIA Correction) and Antarctica (Without GIA Correction) With Trends Calculated Using JPL RL05M Mascons With the Same Time Frame

Study	Time Frame	Antarctica Trend (Gt/yr)		Greenland Trend (Gt/yr)	
		Study	JPL RL05M	Study	JPL RL05M
<i>Barletta et al.</i> [2013]	Jan 2003 to Nov 2011	$-12 \pm 36$	$-58 \pm 21$	$-234 \pm 20$	$-257 \pm 29$
<i>Jacob et al.</i> [2012]	Jan 2003 to Dec 2010	$-23 \pm 16$	$-54 \pm 21$	$-222 \pm 9$	$-244 \pm 29$
<i>Luthcke et al.</i> [2013]	Dec 2003 to Dec 2010	$-34 \pm 19$	$-67 \pm 21$	$-230 \pm 12$	$-249 \pm 29$
<i>Sasgen et al.</i> [2012]	Oct 2003 to Oct 2009	---	---	$-238 \pm 29$	$-235 \pm 29$
<i>Sasgen et al.</i> [2013]	Jan 2003 to Sep 2012	$-61 \pm 23$	$-56 \pm 21$	---	---
<i>Schrama et al.</i> [2014]	Feb 2003 to Jun 2013	$-39 \pm 18$	$-60 \pm 21$	$-278 \pm 19$	$-285 \pm 29$
<i>Shepherd et al.</i> [2012]	Jan 2003 to Dec 2010	$-26 \pm 30$	$-54 \pm 21$	$-230 \pm 27$	$-244 \pm 29$
<i>Velicogna and Wahr</i> [2013]	Jan 2003 to Nov 2012	$-12 \pm 35$	$-56 \pm 21$	$-258 \pm 41$	$-273 \pm 29$

*A et al.* [2013], which uses ICE-5G [Peltier, 2004] for loading history and features a compressible Earth model. This GIA model results in a correction to the trend of +4 Gt/yr for Greenland. For Antarctica, Table 4 does not include a GIA correction, as mentioned above, but for a complete mass balance estimate, we would correct the GRACE data using the regional IJ05\_R2 model [Ivins et al., 2013], which changes the trend by  $-61$  Gt/yr. This would, for instance, mean that the mass balance for Antarctica from February 2003 to June 2013 is  $-121$  Gt/yr as calculated with the JPL RL05M mascons.

Table 4 shows that the JPL mascon solutions provide mass loss rates which are consistently higher than previously published results, but not enough to be outside of the formal error bars of the solution uncertainties. For Greenland, the mascons agree most closely with *Sasgen et al.* [2012], to within 3 Gt/yr, as well as *Schrama et al.* [2014], to within 7 Gt/yr. For Antarctica, the best agreement for ice mass loss is found with *Sasgen et al.* [2013], to within 5 Gt/yr; however, our solution agrees with all studies to within the formal uncertainties. In general, this widespread agreement between solutions reinforces the notion expressed by *Shepherd et al.* [2012] that as techniques are being refined, agreement is being reached on the rate of mass loss for the entire ice sheets. Future work should involve performing comparisons at smaller spatial scales to better understand basin variability of mass balance, such as a mascon by mascon comparison with *Luthcke et al.* [2013].

Rather than rigorously deriving formal uncertainty values for our trend estimates in Table 4, we use values provided by *Velicogna and Wahr* [2013], where all error sources (including atmosphere and ocean effects) were carefully considered. The main difference is that the mascon solutions do not have the same scaling uncertainty as reported in *Velicogna and Wahr* [2013], and we have updated the error estimates in the mascon solutions to reflect this.

## 8. Discussion

We have developed new GRACE gravity products using updated background models and updated Level 1 data, and expressed the result in unconstrained harmonics and by using spherical cap mass concentration blocks as a basis function and carefully introducing geophysically based a priori information into the inversion to minimize errors without biasing the solutions toward a particular model. We find the RL05 harmonics to be improved over previous generations of harmonic solutions and the a priori conditioned mascon solution to provide considerable advances over existing methods. A major advantage to this solution over traditional unconstrained spherical harmonic gravity solutions is that it eliminates the burden on the user to apply empirical postprocessing filters to remove correlated errors in the gravity solutions. It also eliminates the need for sophisticated averaging techniques to resolve mass loss rates from Greenland, for instance. Together, these improvements make the resulting gravity solutions significantly more “user friendly.”

The primary disadvantage to the mascon technique is that it is not straightforward to quantify potential signal suppression that occurs due to the addition of the a priori information. We note, however, that it is also difficult to quantify the exact amount of signal suppression that occurs when applying empirical postprocessing algorithms to remove correlated errors in the spherical harmonic gravity solutions; derived scale factors are merely a good proxy for this and have considerable spatial variability in effect. Although improvements can be made in the details of the implementation, such as including deterministic geophysical

processes (such as trends and annual signals) as state parameters and using smaller mascons to more accurately define coastlines (similar to *Luthcke et al.* [2013]) and spatial constraints, we argue in the spirit of optimal filtering theory that the introduction of credible statistical geophysical information (either from models or from independent observations) to condition the solution when solving for gravity anomalies, as done in this study, is ultimately preferable to relying on empirical ad hoc postprocessing techniques to remove correlated errors.

An additional improvement over conventional harmonic solutions is that the mascon solutions rely less on empirical scale factors to gain accurate mass estimates in river basins (which should also be true for glacial drainage basins in Greenland and Antarctica). This is beneficial since the addition of scale factors can have significant uncertainty, in particular for determining surface mass variations on longer than annual timescales. Thus, the mascon solutions should allow for improved spatial resolution and accuracy when studying trends in smaller-scale glacial and hydrological basins. Finally, our results indicate that the mascon solutions will allow for the first time the study of low-latitude ocean signals where the signal magnitude is very small.

# Acknowledgments

The research described in this paper was carried out at the Jet Propulsion Laboratory, California Institute of Technology, under a contract with the National Aeronautics and Space Administration. The JPL RL05 and RL05M solutions are available via the Physical Oceanography Distributed Active Archive Center (PODAAC) as well as the GRACE Tellus websites.

# References

- A, G., J. Wahr, and S. Zhong (2013), Computations of the viscoelastic response of a 3-D compressible Earth to surface loading: An application to Glacial Isostatic Adjustment in Antarctica and Canada, *Geophys. J. Int.*, *192*, 557–572, doi:10.1093/gji/ggs030.
- Barletta, V. R., L. S. Sørensen, and R. Forsberg (2013), Scatter of mass change estimates at basin scale for Greenland and Antarctica, *Cryosphere*, *7*, 1411–1432, doi:10.5194/tc-7-1411-2013.
- Baur, O., M. Kuhn, and W. E. Featherstone (2009), GRACE-derived ice-mass variations over Greenland by accounting for leakage effects, *J. Geophys. Res.*, *114*, B06407, doi:10.1029/2008JB006239.
- Böning, C. (2009), Validation of ocean mass variability derived from the Gravity Recovery and Climate Experiment—Studies utilizing in-situ observations and results from a Finite Element Sea Ice-Ocean Model, Bremen, Univ., Diss.
- Böning, C., R. Timmermann, A. Macrandner, and J. Schröter (2008), A pattern-filtering method for the determination of ocean bottom pressure anomalies from GRACE solutions, *Geophys. Res. Lett.*, *35*, L18611, doi:10.1029/2008GL034974.
- Bruinsma, S., J. M. Lemoine, R. Biancale, and N. Vales (2010), CNES/GRGS 10-day gravity field models (release 2) and their evaluation, *Adv. Space Res.*, *45*(4), 587–601, doi:10.1016/j.asr.2009.10.012.
- Case, K., G. Kruizinga, and S. C. Wu (2010), GRACE level 1B data product user handbook, Jet Propul. Lab., Calif. Inst. of Technol., JPL D-22027.
- Chambers, D. P. (2006), Observing seasonal steric sea level variations with GRACE and satellite altimetry, *J. Geophys. Res.*, *111*, C03010, doi:10.1029/2005JC002914.
- Chen, J. L., C. R. Wilson, and B. D. Tapley (2011), Interannual variability of Greenland ice losses from satellite gravimetry, *J. Geophys. Res.*, *116*, B07406, doi:10.1029/2010JB007789.
- Cheng, M., and B. D. Tapley (2004), Variations in the Earth's oblateness during the past 28 years, *J. Geophys. Res.*, *109*, B09402, doi:10.1029/2004JB003028.
- Crétaux, J.-F., et al. (2011), SOLS: A lake database to monitor in the near real time water level and storage variations from remote sensing data, *Adv. Space Res.*, *47*, 1497–1507, doi:10.1016/j.asr.2011.01.004.
- Desai, S. D., and D.-N. Yuan (2006), Application of the convolution formalism to the ocean tide potential: Results from the Gravity Recovery and Climate Experiment (GRACE), *J. Geophys. Res.*, *111*, C06023, doi:10.1029/2005JC003361.
- Desai, S. D., W. Bertiger, J. Gross, B. Haines, N. Harvey, C. Selle, A. Sibthorpe, and J. P. Weiss (2011), Results from the reanalysis of global GPS data in the IGS08 reference frame, AGU Fall Meeting, San Francisco, Calif.
- Dobslaw, H., F. Flechtner, I. Bergmann-Wolf, C. Dahle, R. Dill, S. Esselborn, I. Sasgen, and M. Thomas (2013), Simulating high-frequency atmosphere-ocean mass variability for de-aliasing of satellite gravity observations: AOD1B RL05, *J. Geophys. Res. Oceans*, *118*, 3704–3711, doi:10.1002/jgrc.20271.
- Famiglietti, J. S., M. Lo, S. L. Ho, J. Bethune, K. J. Anderson, T. H. Syed, S. C. Swenson, C. R. de Linage, and M. Rodell (2011), Satellites measure recent rates of groundwater depletion in California's Central Valley, *Geophys. Res. Lett.*, *38*, L03403, doi:10.1029/2010GL046442.
- Flechtner, F. (2007), AOD1b product description document for product releases 01 to 04, GRACE 327–750, GeoForschungszentrum Potsdam, Potsdam, Germany.
- Folkner, W. M., J. A. Steppe, and S. H. Oliveau (1993), Earth orientation parameter file description and usage, *Interoffice Memo*. 335.1-11-93, Jet Propul. Lab., Calif. Inst. of Technol., Pasadena, Calif.
- Folkner, W. M., J. G. Williams, and D. H. Boggs (2009), The planetary and lunar Ephemeris DE 421, IPN Progress Report 42–178, Aug. 2009.
- Han, S.-C., R. Riva, J. Sauber, and E. Okal (2013), Source parameter inversion for recent great earthquakes from a decade-long observation of global gravity fields, *J. Geophys. Res. Solid Earth*, *118*, 1240–1267, doi:10.1002/jgrb.50116.
- Heiskanen, W., and H. Moritz (1967), *Physical Geodesy*, W. H. Freeman, San Francisco, Calif.
- Higham, N. J. (2002), Computing the nearest correlation matrix—A problem from finance, *IMA J. Numer. Anal.*, *22*, 329–343, doi:10.1093/imanum/22.3.329.
- Holdridge, D. B. (1967), An alternate expression for light time using general relativity, JPL Space Program Summary 37–48, III, pp. 2–4.
- Houborg, R., M. Rodell, B. Li, R. Reichle, and B. Zaitchik (2012), Drought indicators based on model assimilated GRACE terrestrial water storage observations, *Water Resour. Res.*, *48*, W07525, doi:10.1029/2011WR011291.
- Ivins, E. R., M. M. Watkins, D.-N. Yuan, R. Dietrich, G. Casassa, and A. Rulke (2011), On-land ice loss and glacial isostatic adjustment at the Drake Passage: 2003–2009, *J. Geophys. Res.*, *116*, B02403, doi:10.1029/2010JB007607.
- Ivins, E. R., T. S. James, J. Wahr, E. J. O. Schrama, F. W. Landerer, and K. M. Simon (2013), Antarctic contribution to sea-level rise observed by GRACE with improved GIA correction, *J. Geophys. Res. Solid Earth*, *118*, 3126–3141, doi:10.1002/jgrb.50208.
- Jacob, T., J. Wahr, W. T. Pfeffer, and S. Swenson (2012), Recent contributions of glaciers and ice caps to sea level rise, *Nature*, *482*, 514–518, doi:10.1038/nature10847.



- Kanzow, T., F. Flechtner, A. Chave, R. Schmidt, P. Schwintzer, and U. Send (2009), Seasonal variation of ocean bottom pressure derived from Gravity Recovery and Climate Experiment (GRACE): Local validation and global patterns, *J. Geophys. Res.*, **110**, C09001, doi:10.1029/2004JC002772.
- Kaula, W. M. (1966), *Theory of Satellite Geodesy*, Blaisdell Pub. Co., Waltham, Mass.
- Kim, J. (2000), Simulation study of a low-low satellite-to-satellite tracking mission, PhD thesis, The Univ. of Texas at Austin.
- Kurtenbach, E., T. Mayer-Gürr, and A. Eicker (2009), Deriving daily snapshots of the Earth's gravity field from GRACE L1B data using Kalman filtering, *Geophys. Res. Lett.*, **36**, L17102, doi:10.1029/2009GL039564.
- Landerer, F. W., and S. C. Swenson (2012), Accuracy of scaled GRACE terrestrial water storage estimates, *Water Resour. Res.*, **48**, W04531, doi:10.1029/2011WR011453.
- Long, D., B. R. Scanlon, L. Longuevergne, A.-Y. Sun, D. N. Fernando, and H. Save (2013), GRACE satellites monitor large depletion in water storage in response to the 2011 drought in Texas, *Geophys. Res. Lett.*, **40**, 3395–3401, doi:10.1002/grl.50655.
- Luthcke, S. B., H. J. Zwally, W. Abdalati, D. D. Rowlands, R. D. Ray, R. S. Nerem, F. G. Lemoine, J. J. McCarthy, and D. S. Chinn (2006a), Recent Greenland ice mass loss by drainage system from satellite gravity observations, *Science*, **314**, 1286–1289, doi:10.1126/science.1130776.
- Luthcke, S. B., D. D. Rowlands, F. G. Lemoine, S. M. Klosko, D. Chinn, and J. J. McCarthy (2006b), Monthly spherical harmonic gravity field solutions determined from GRACE inter-satellite range-rate data alone, *Geophys. Res. Lett.*, **33**, L02402, doi:10.1029/2005GL024846.
- Luthcke, S. B., T. J. Sabaka, B. D. Loomis, A. A. Arendt, J. J. McCarthy, and J. Camp (2013), Antarctica, Greenland, and Gulf of Alaska land-ice evolution from an iterated GRACE global mascon solution, *J. Glaciol.*, **59**(216), doi:10.3189/2013JoG12J147.
- Macrander, A., C. Böning, O. Boebel, and J. Schröter (2010), GRACE Validation by in-situ data of Ocean Bottom Pressure, in *Satellite Geodesy and Earth System Science*, edited by F. Flechtner et al., Part 2, pp. 169–185, Springer, Berlin, Heidelberg, doi:10.1007/978-3-642-10228-8\_14.
- Menemenlis, D., J. Campin, P. Heimbach, C. Hill, T. Lee, A. Nguyen, M. Schodlock, and H. Zhang (2008), ECCO2: High resolution global ocean and sea ice data synthesis, *Mercator Ocean Quart. Newsl.*, **31**, 13–21.
- Montenbruck, O., M. Garcia-Fernandez, Y. Yoon, S. Schön, and A. Jäggi (2009), Antenna phase center calibration for precise positioning of LEO satellites, *GPS Solution*, **13**(1), 23–34.
- Morison, J., J. Wahr, R. Kwok, and C. Peralta-Ferriz (2007), Recent trends in Arctic Ocean mass distribution revealed by GRACE, *Geophys. Res. Lett.*, **34**, L07602, doi:10.1029/2006GL029016.
- Moyer, T. D. (1971), Mathematical formulation of the Double-Precision Orbit Determination Program, *Tech. Rep. 32–1527*, Jet Propul. Lab., Calif. Inst. of Technol., Pasadena, Calif.
- Moyer, T. D. (2000), Formulation for observed and computed values of deep space network types for navigation, JPL Publ., 00–7.
- Muller, P., and W. L. Sjogren (1968), Mascons: Lunar mass concentrations, *Science*, **161**, 680.
- Park, J.-H., D. R. Watts, K. A. Donohue, and S. R. Jayne (2008), A comparison of in situ bottom pressure array measurements with GRACE estimates in the Kuroshio Extension, *Geophys. Res. Lett.*, **35**, L17601, doi:10.1029/2008GL034778.
- Paulson, A., S. Zhong, and J. Wahr (2007), Inference of mantle viscosity from GRACE and relative sea level data, *Geophys. J. Int.*, **171**, 497–508, doi:10.1111/j.1365-246X.2007.03556.x.
- Peltier, W. R. (2004), Global glacial isostasy and the surface of the ice-age Earth: The ICE-5G (VM2) model and GRACE, *Annu. Rev. Earth Planet. Sci.*, **32**, 111–149, doi:10.1146/annurev.earth.32.082503.144359.
- Petit, G., and B. Luzum (Eds.) (2010), IERS Conventions (2010), IERS Convention Centre, IERS Tech. Note 36.
- Qi, H.-D., and D. Sun (2006), A quadratically convergent Newton method for computing the nearest correlation matrix, *SIAM J. Matrix Anal. Appl.*, **28**, 360–386, doi:10.1137/050624509.
- Ray, R. (1999), A global ocean tide model from Topex/Poseidon altimetry: GOT 99.2, NASA Tech Memo 209478: 58.
- Ries, J. C., S. Bettadpur, S. Poole, and T. Richter (2011), Mean background gravity fields for GRACE processing, GRACE Science Team Meeting, Austin, Tex.
- Rietbroek, R., P. LeGrand, B. Wouters, J.-M. Lemoine, G. Ramillien, and C. W. Hughes (2006), Comparison of in situ bottom pressure data with GRACE gravimetry in the Crozet-Kerguelen region, *Geophys. Res. Lett.*, **33**, L21601, doi:10.1029/2006GL027452.
- Rodell, M., et al. (2004), The global land data assimilation system, *Bull. Am. Meteorol. Soc.*, **85**, 381–394.
- Rodell, M., I. Velicogna, and J. S. Famiglietti (2009), Satellite-based estimates of groundwater depletion in India, *Nature*, **460**, 999–1002, doi:10.1038/nature08238.
- Rowlands, D. D., S. B. Luthcke, J. J. McCarthy, S. M. Klosko, D. S. Chinn, F. G. Lemoine, J.-P. Boy, and T. B. Sabaka (2010), Global mass flux solutions from GRACE: A comparison of parameter estimation strategies-Mass concentrations versus Stokes coefficients, *J. Geophys. Res.*, **115**, B01403, doi:10.1029/2009JB006546.
- Sabaka, T. J., D. D. Rowlands, S. B. Luthcke, and J.-P. Boy (2010), Improving global mass flux solutions from Gravity Recovery and Climate Experiment (GRACE) through forward modeling and continuous time correlation, *J. Geophys. Res.*, **115**, B11403, doi:10.1029/2010JB007533.
- Sasgen, I., M. van den Broeke, J. L. Bamber, E. Rignot, L. S. Sørensen, B. Wouters, Z. Martinec, I. Velicogna, and S. B. Simonsen (2012), Timing and origin of recent regional ice-mass loss in Greenland, *Earth Planet. Sci. Lett.*, **333–334**, 293–303, doi:10.1016/j.epsl.2012.03.033.
- Sasgen, I., H. Konrad, E. R. Ivins, M. R. Van den Broeke, J. L. Bamber, Z. Martinec, and V. Klemann (2013), Antarctic ice-mass balance 2003 to 2012: Regional reanalysis of GRACE satellite gravimetry measurements with improved estimate of glacial-isostatic adjustment based on GPS uplift rates, *Cryosphere*, **7**, 1499–1512, doi:10.5194/tc-7-1499-2013.
- Save, H., S. Bettadpur, and B. D. Tapley (2012), Reducing errors in the GRACE gravity solutions using regularization, *J. Geod.*, doi:10.1007/s00190-012-0548-5.
- Schrama, E. J. O., and B. Wouters (2011), Revisiting Greenland ice sheet mass loss observed by GRACE, *J. Geophys. Res.*, **116**, B02407, doi:10.1029/2009JB006847.
- Schrama, E. J. O., B. Wouters, and R. Rietbroek (2014), A mascon approach to assess ice sheet and glacier mass balances and their uncertainties from GRACE data, *J. Geophys. Res. Solid Earth*, **119**, 6048–6066, doi:10.1002/2013JB010923.
- Shepherd, A., et al. (2012), A reconciled estimate of ice-sheet mass balance, *Science*, **338**(6111), 1183–1189, doi:10.1126/science.1228102.
- Sunseri, R. (2010), Mass concentration modeled as a spherical cap, Interoffice Memorandum, 343R-11-00.
- Swenson, S., and J. Wahr (2006), Post-processing removal of correlated errors in GRACE data, *Geophys. Res. Lett.*, **33**, L08402, doi:10.1029/2005GL025285.
- Swenson, S., D. Chambers, and J. Wahr (2008), Estimating geocenter variations from a combination of GRACE and ocean model output, *J. Geophys. Res.*, **113**, B08410, doi:10.1029/2007JB005338.
- Tapley, B. D., B. E. Schutz, and G. H. Born (2004), *Statistical Orbit Determination*, Elsevier Inc., San Diego, Calif.
- Tiwari, V. M., J. Wahr, and S. C. Swenson (2009), Dwindling groundwater resources in northern India, from satellite gravity observations, *Geophys. Res. Lett.*, **36**, L18401, doi:10.1029/2009GL039401.
- Velicogna, I. (2009), Increasing rates of ice mass loss from the Greenland and Antarctic ice sheets revealed by GRACE, *Geophys. Res. Lett.*, **36**, L19503, doi:10.1029/2009GL040222.



- Velicogna, I., and J. Wahr (2013), Time-variable gravity observations of ice sheet mass balance: Precision and limitations of the GRACE satellite data, *Geophys. Res. Lett.*, **40**, 3055–3063, doi:10.1002/grl.50527.
- Velicogna, I., T. C. Sutterley, and M. R. van den Broeke (2014), Regional acceleration in ice mass loss from Greenland and Antarctica using GRACE time-variable gravity data, *J. Geophys. Res. Space Physics*, **119**, 8130–8137, doi:10.1002/2014GL061052.
- Wahr, J., M. Molenaar, and F. Bryan (1998), Time variability of the Earth's gravity field: Hydrological and oceanic effects and their possible detection using GRACE, *J. Geophys. Res.*, **103**, 30, 205–30, 229, doi:10.1029/98JB02844.
- Watkins, M., D. Yuan, D. Kuang, W. Bertiger, M. Kim, and G. Kruizinga (2005), GRACE harmonic and mascon solutions at JPL, *Eos Trans. AGU*, **86**(52), Fall Meet. Suppl., Abstract G22A-04, San Francisco, Calif.
- Watkins, M. M., and D.-N. Yuan (2012), GRACE JPL Level-2 processing standards document for level-2 product release 05, GRACE 327–744 (v 5.0).
- Wiese, D. N., M. M. Watkins, F. W. Landerer, and D.-N. Yuan (2013), Post-processing methods with applications to JPL RL05M GRACE mascon solutions, AGU Fall Meeting, San Francisco, Calif., 9–13 Dec.
- Wong, L., G. Buechler, W. Downs, W. Sjogren, P. Muller, and P. Gottlieb (1971), A surface-layer representation of the lunar gravitational field, *J. Geophys. Res.*, **76**(26), 6220–6236, doi:10.1029/JB076i026p06220.
- Wu, S.-C., G. Kruizinga, and W. Bertiger (2006), Algorithm theoretical basis document for GRACE level-1B data processing V1.2, GRACE 327–741 (JPL D-27672).
- Yuan, D.-N. (1991), The determination and error assessment of the Earth's gravity field model, PhD thesis, Univ. of Texas at Austin.